MODELING OF FRICTION STIRRING

by

Mohamed Anass Abdalla Badreldin

A Thesis presented to the Faculty of the
American University of Sharjah
College of Engineering
In Partial Fulfillment
of the Requirements
for the Degree of

Master of Science in
Mechanical Engineering

Sharjah, United Arab Emirates

November 2018

Approval Signatures

We, the undersigned, approve the Master's Thesis of Mohamed Anass Abdalla Badreldin.

Thesis Title: Modeling of Friction Stirring

Signature	**Date of Signature** (dd/mm/yyyy)
_____	_____
Dr. Mohammad Nazzal Associate Professor, Department of Mechanical Engineering Thesis Advisor	
_____	_____
Dr. Basil Darras Associate Professor, Department of Mechanical Engineering Thesis Co-Advisor	
_____	_____
Dr. Maen Alkhader Associate Professor, Department Mechanical Engineering Thesis Committee Member	
_____	_____
Dr. Mohammad AlHamaydeh Associate Professor, Department of Civil Engineering Thesis Committee Member	
_____	_____
Dr. Mamoun Abdel-Hafez Head, Department of Mechanical Engineering	
_____	_____
Dr. Ghaleb Husseini Associate Dean for Graduate Affairs and Research College of Engineering	
_____	_____
Dr. Richard Schoephoerster Dean, College of Engineering	
_____	_____
Dr. Mohamed El-Tarhuni Vice Provost for Graduate Studies	

Acknowledgement

I would like to thank ALLAH for blessing me and giving me the opportunity to study and complete my graduate studies at AUS.

I would like to express the deepest appreciation to the AUS Graduate office for granting me a full assistantship. Also, I would also express my gratitude to my kind advisors, Dr. Mohammad Nazzal and Dr. Basil Darras for their continuous guidance, help, and support.

I am grateful to my mother Manal and my father, who has continuously provided emotional and moral support. A special gratitude goes to my dear wife, Wisal Siyam, who supported me throughout my graduate studies at AUS and for making my difficult days easier.

Abstract

The last two decades have witnessed significant advances in friction stir welding (FSW). This solid-state welding process was originally used for joining Aluminum alloys before being extended to other metallic and non-metallic materials. The high complexity in FSW stems from the complex interactions between highly coupled physical phenomena. As experimental procedures are costly and time-consuming, numerical simulations were used extensively in an effort to develop a comprehensive understanding of the process. This research consists of two parts: one part provides a critical review of the three fundamental components of the numerical simulation of FSW; which are the numerical method, the constitutive model, and the contact model. The second part contains the detailed development of the finite element model to study the FSW process and submerged FSW process (SFSW), with emphasis on the effect of submerging on the temperature profile and thermal history. The finite element model is developed using the Coupled Eulerian-Lagrangian modeling technique and is validated against previous experimental work for the Aluminum 5083 alloy. Temperature profiles for different welding conditions are investigated to validate the model. The developed finite element model is able to predict the temperature profile in both FSW and SFSW processes. It also captures the dissymmetrical temperature distribution around the welding line; and the effect of using the SFSW process on peak temperatures, cooling rates, and size of the heat affected zone. Moreover, flash formation and the material flow patterns are successfully captured. The results show that increasing the rotational speed from 1000 rpm to 1700 rpm for the SFSW of the Aluminum 5083 alloy resulted in an increase in peak temperature by 200%. This temperature rise yields to material softening, improved the material flow, and higher weld quality.

Search Terms: ***Friction Stir Welding, Johnson-Cook Model, Submerged Friction Stir Welding, Coupled Eulerian-Lagrangian modeling, Heat transfer, Numerical Modeling.***

Table of Contents

List of Figures

Chapter 1. Introduction

In 1991, The Welding Institute (TWI) (Cambridge, United Kingdom) invented a solid-state joining process called Friction Stir Welding. This process uses a third body tool to join two similar or dissimilar materials without melting them. The joining process is achieved by rotating a non-consumable cylindrical tool with a specifically designed shoulder and probe. The tool is radially plunged at a constant rate into the joint (Figure 1.1). Consequently, due to the frictional contact between the tool and workpiece, frictional heat is generated. The frictional heat plus the heat generated due to plastic deformation, along with the adiabatic heat within the material, lead to material softening without melting [1]. After the tool probe is completely plunged into the joint, the tool is moved in the transverse direction developing a highly characteristic welding zone. The side of the weld at which the tool's feed velocity and tangential velocity are additive is designated as the advancing side. At the retreating side, the tangential tool's feed velocity and tangential velocity are opposite as shown in Figure 1.1.

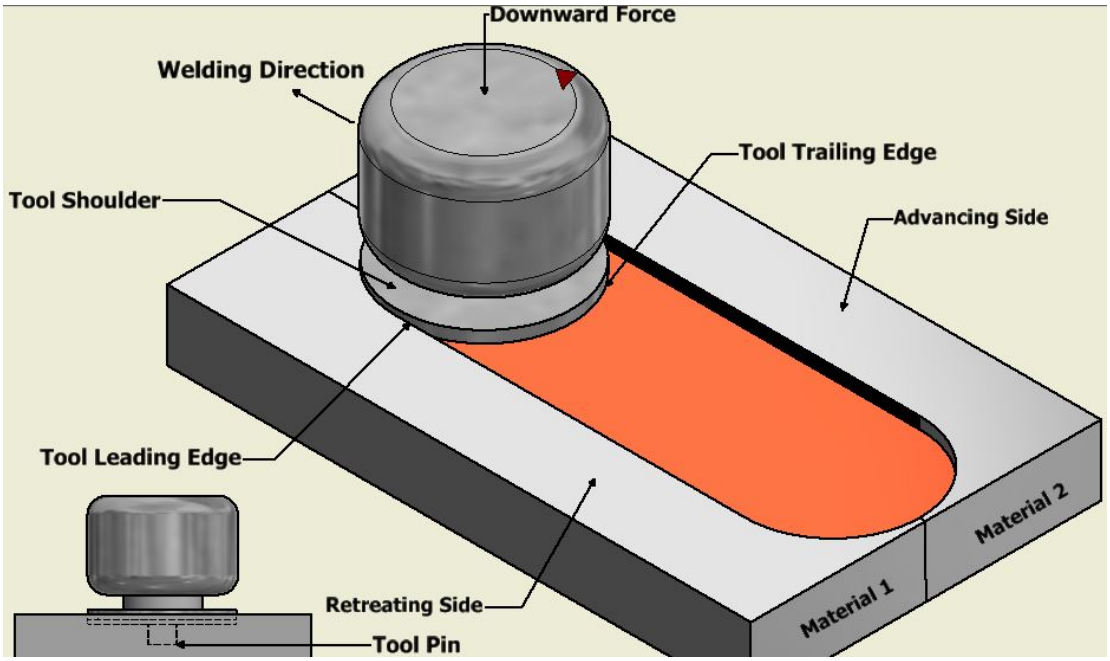

Figure 1.1 Sketch Drawing of FSW Arrangement

FSW has several advantages when compared to conventional welding methods. As FSW is a solid-state process, it does not require shielding gases or flux and it avoids common problems of fusion welding such as weld porosity, hot cracking, and lack of

fusion. It consumes less energy when compared to fusion welding processes, and it generates no fumes or pollutants. In addition, thermal and mechanical tensioning can control residual stresses. The intense plastic deformation at a high temperature in the weld zone results in fine equiaxed recrystallized grains that yield to excellent mechanical properties [1-5]. Based on Friction Stir Welding (FSW), Friction Stir Processing (FSP) emerged as a tool for microstructural modification [1]. In FSP, the rotating tool is inserted in a monolithic workpiece to provide localized modification and control of the microstructure for specific property enhancement. Other variants of FSW are Friction Stir Spot Welding, Friction Stir Back Extrusion, Micro FSW, Ultra-Sonic Vibration Enhanced FSW.

The FSW/FSP is a very complex process that includes complex interactions between different thermomechanical processes like frictional heat dissipation, heat dissipation due to plastic deformation, the flow of material, local cooling, and dynamic recrystallization. As a result, the welded material undergoes severe plastic deformation and dynamic recrystallization. Moreover, the FSW process is considered a high strain rate process; strain rates to 10 s^{-1} were recorded in previous studies [2, 6-8].

Recent advancements in high-performance computing and numerical algorithms have led to increased usage of numerical simulations for modeling the FSW process. Numerical simulations provide an effective tool to investigate the behavior of nonlinear physical systems that have complex mathematical models; FSW and its variants are typical cases. Benefits of numerical simulations include lower cost and time saving when compared to experiments. Fewer assumptions and more realistic mathematical description are applied when compared to analytical methods.

Due to the non-linearity and highly complex interactions in the FSW process, several researchers [9-16] attempted to simulate FSW numerically in an effort to understand the material flow and the effects of process parameters on the different aspects of the FSW process. The general framework of the numerical simulation of FSP is shown in Figure 1.2. Numerical simulations start by observing the physical phenomena and establishing the mathematical models that are expressed in terms of governing and constitutive equations with the proper initial and boundary conditions. Then the governing equations; represented in most cases in the form of partial differential equations, are solved numerically. The numerical method generally

includes domain discretization, numerical discretization, and the numerical routine used to solve the resulting set of algebraic or ordinary differential equations.

The numerical method plays a very important role in the accuracy of the computational results and computational cost. In this work, the numerical methods used in literature to simulate FSW are classified based on whether a Lagrangian approach or a Eulerian approach is used. The Eulerian approach has been used in most of the CFD codes. On the other hand, in the meshfree methods, the continuum is discretized using a finite number of discrete particles that interact without mesh constraints. Several researchers [17-21] used meshfree methods to simulate FSW because of its native ability to model large deformation and determine the time history of all the field variables for any particle in the continuum.

Numerical simulations in solid mechanics can be considered reliable only when a proper constitutive model that describes the material behavior is used. Johnson-cook model, Sellars and Tegart model, Zerilli Armstrong model, and other models have been used in the literature due to their ability to capture the effect of strain, strain rate, and temperature on the flow stress of the material. As the FSW is a coupled thermo-mechanical process, the effect of heat generation on the flow behavior should also be considered. Heat generated during FSW is highly dependent on contact conditions at the tool-workpiece interface. Several mechanical friction models have been used to characterize the contact conditions using numerical simulations. Columb, Tresca, Columb limited by Tresca, and the Viscoplastic Friction Law are the most commonly used models in the literature.

The aim of this research can be summarized in two points: first, to provide a critical review on the three main building blocks for numerical simulation of FSW that are the numerical method, the constitutive model, and the mechanical friction model. In each section, the current state of the art is presented along with a critical comparison between different methods and models. The review will be based on literature related to numerical simulations of FSW and FSP of metals.

Second, to create a finite element model that is able to capture temperature distribution, material flow and the effect of submerging the process underwater in temperature distribution. The model is validated against the experimental work done by Kishta and Darras [22].

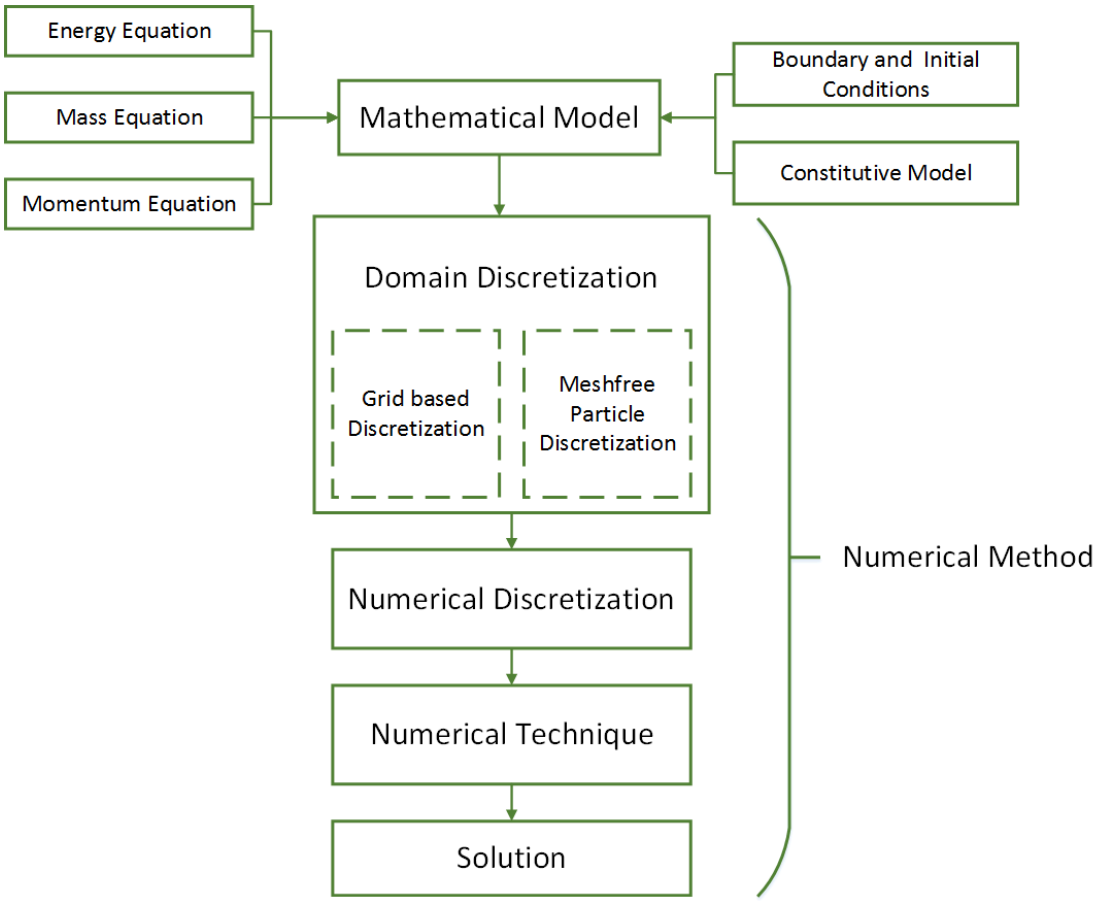

Figure 1.2 General framework for conducting numerical simulations in FSW

Chapter 2. Eulerian Approach

2.1. Description of Motion and Governing Equations

In the Eulerian approach, the integration domain (mesh/grid) is defined in a Eulerian reference system R_x that remains fixed (inertial system) while the continuum moves across the fixed mesh. The nodes are defined as spatial points in space and the velocity of the mesh $v_{mesh} = 0$. The fundamental property in the Eulerian framework is the velocity field $v(x,t)$; where x is a spatial point (coordinate of a point in space) defined in the fixed Cartesian domain R_x and t is the time. On the other hand, in the Lagrangian approach, the integration domain (grid/mesh) is defined in a material reference system $R_X$where the grid is attached to the material and deforms with it.

To apply the conservation laws in the Eulerian reference frame, the material derivative (the rate of change of a property following a fluid particle) in terms of Eulerian quantities should be evaluated. The material derivative is defined as follows:

$$\frac{D}{Dt} = \left.\frac{\partial}{\partial t}\right|_x + \boldsymbol{v}.\boldsymbol{\nabla_x} \tag{1}$$

where $\frac{D}{Dt}$ is the material derivative, $\left.\frac{\partial}{\partial t}\right|_x$ is the spatial derivative (time rate of change at a given fixed point), $\boldsymbol{v} = \frac{\partial \boldsymbol{x}(\boldsymbol{X},t)}{\partial t}$ is the spatial velocity, $\boldsymbol{\nabla_x} = \frac{\partial}{\partial \boldsymbol{x}}$ is the spatial gradient. The second term $\boldsymbol{v}.\boldsymbol{\nabla_x}$ is the convective derivative, which is the time rate of change due to the movement of the material element from one location to another where the flow properties are spatially different.

The governing conservation equations in PDE form in the spatial domain R_x consisting of spatial points x for the Eulerian description are [23]:

Mass
$$\frac{D\rho}{Dt} = \left.\frac{\partial \rho}{\partial t}\right|_x + \boldsymbol{v}.\boldsymbol{\nabla_x}\rho = -\rho \boldsymbol{\nabla_x}.\boldsymbol{v}$$

Momentum
$$\rho\frac{D\boldsymbol{v}}{Dt} = \rho\left(\left.\frac{\partial v}{\partial t}\right|_x + (\boldsymbol{v}.\boldsymbol{\nabla_x})\boldsymbol{v}\right) = \boldsymbol{\nabla_x}.\boldsymbol{\sigma} + \rho\boldsymbol{b} \tag{2}$$

Energy
$$\rho\frac{DE}{Dt} = \rho\left(\left.\frac{\partial E}{\partial t}\right|_x + \boldsymbol{v}.\boldsymbol{\nabla_x}\boldsymbol{E}\right) = \boldsymbol{\nabla_x}.(\boldsymbol{\sigma}.\boldsymbol{v}) + \boldsymbol{v}.\rho\boldsymbol{b}$$

where ρ is the mass density, $\boldsymbol{\sigma}$ denotes the Cauchy stress tensor, $\boldsymbol{b}$ is the specific body force vector, and E is the specific total energy.

The current position of a particle X can be determined as follows [24]:

$$\boldsymbol{x}(\boldsymbol{X}, t) = \boldsymbol{X} + \int_0^t \boldsymbol{v}(\boldsymbol{X}, t)dt \tag{3}$$

where $\boldsymbol{x}(\boldsymbol{X}, t)$is the current position of a particle, $\boldsymbol{X}$ is the reference position of the particle at $\boldsymbol{t} = \boldsymbol{0}$**.** Several researchers [12, 25-33] used the Eulerian approach along with the Finite Volume Method (FVM) to discretize the governing equations and simulate the FSW process. This approach is employed in majority of the CFD commercial codes. Details about the results obtained using CFD codes will be presented in section 2.4.

2.2. Material Constitutive Model

In the Eulerian approach, the material is modeled as an incompressible highly viscous non-Newtonian fluid. Nandan et al. [28], Kim et al. [27], Hasan et al. [26], Colegrove et al. [12], Aljoaba et al. [34], and Pal & Phaniraj [30] defined viscosity as a function of temperature and strain rate. They used Perzyna viscoplasticity model that defines the dynamic viscosity in terms of the effective flow stress and the effective strain rate:

$$\mu = \frac{\sigma(T, \bar{\dot{\varepsilon}})}{3\bar{\dot{\varepsilon}}} \tag{4}$$

where σ is the effective stress, which needs to be determined using a solid-based constitutive relation, and $\bar{\dot{\varepsilon}}$ is the effective strain rate.

The constitutive relation for calculating the viscosity is based on the Sellars and Tegart [35] model used in hot working processes:

$$\sigma_e = \sigma_R sinh^{-1}\left[(\frac{Z}{\beta})^{1/m}\right] \tag{5}$$

where σ_R, β, m are material constants. Z is the Zener-Hollomon parameter, defined as:

$$Z = \dot{\varepsilon}_e \exp(\frac{Q}{RT}) \tag{6}$$

where Q is the activation energy of the material, and R is the universal gas constant.

The effective strain rate is given by [28]:

$$\bar{\dot{\varepsilon}} = (\frac{2}{3}\ \dot{\varepsilon}_{ij}\dot{\varepsilon}_{ij})^{1/2} \tag{7}$$

where the strain rate tensor $\dot{\varepsilon}_{ij}$ is given by:

$$\dot{\varepsilon}_{ij} = \frac{1}{2}(\frac{\partial u_i}{\partial x_i} + \frac{\partial u_j}{\partial x_j}) \tag{8}$$

Sellars and Tegart model assumes that the flow stress is independent of the plastic strain and equal to the dynamic recrystallization steady state stress. In other words, it assumes stress saturation at a constant strain rate, which might be the case for high-temperature deformation processes. On the other hand, it might neglect and overestimate stresses at low strains [36]. Moreover, Sellars and Tegart model can predict grain size, as the Zener Hollomon parameter is related directly to the average grain size of dynamic recrystallization [37].

Nassar and Khariasheh [29] modified the viscosity term in Perzyna model to account for localized melting due to excessive heating. They assumed that the volume fraction of the liquid phase (f_L) formed during melting increases linearly from zero at the solidus temperature to one at the liquidous temperature according to the following piecewise function:

$$f_L = \begin{cases} 0 & T < T_s \\ \dfrac{T - T_s}{T_L - T_s} & T_s \geq T \geq T_L \\ 1 & T < T_L \end{cases} \tag{9}$$

They assumed that the modified viscosity of the material is:

$$\eta_{total} = f_S \,.\, \eta_S + f_L \,.\, \eta_L \tag{10}$$

$$\eta_{mod} = (1 - f_L) \,.\, \sigma_R \ \sinh^{-1}\left[\left(\frac{\bar{\dot{\varepsilon}} \exp\ (Q/RT)}{A}\right)^{1/n}\right] / 3\bar{\dot{\varepsilon}} \tag{11}$$

where η_L is the melt viscosity and $f_S = 1 - f_L$ is the fraction of the solid phase.

Note that in the previous equations, for the material they used Mg AZ31, at which the viscosity of the liquid is very small compared to that of the solid and therefore can be neglected.

2.3. Contact Conditions and Heat Generation

In the modeling of FSW, it is critically important to define the interface boundary condition at the tool-workpiece interface. Three different contact states; without considering a realistic friction model, are imposed in modeling FSW using the Eulerian approach:

1- Sliding Condition: in this state, the velocity of the matrix material (V matrix) at the interface is zero. This implies that the contact shear stress is less than the matrix yield shear stress.

2- Sticking Condition: In this state, the tool velocity ($V_{tool} = \omega \, . r$) and the martix velocity are identical on the interface, and the contact shear stress is equal to the material yield shear stress. Most studies assumed that a sticking condition exists at the tool-workpiece interface [9, 12, 33, 38-40]. This assumption is not realistic; especially in the shoulder region, and leads to over prediction of the deformed zone. Heat generation is assumed only to be due to plastic deformation without heat generation by friction. Other studies [29] assume sticking condition on the tool's pin interface only.

3- Partial sliding/sticking: In this state, the matrix velocity at the interface is less than the tool velocity. A spatially variable fractional slip (δ) between the tool and the workpiece interface is introduced. If $\delta = 1$, the contact state is pure sliding. If $\delta = 0$, sticking takes place at the interface. In Partial sticking sliding, the contact shear stress is less than or equal to the shear yield stress and the contact state variable is in the range of $0 < \delta < 1$. Based on experimental data of tool workpiece interfacial slip in cross wedge rolling process [41], the contact state variable is expressed as [28]:

$$\delta = 1 - \exp\left(-\frac{1}{\delta_o}\frac{\omega}{\omega_o}\frac{r}{R_s}\right) \tag{12}$$

where δ_o is a constant that is determined by trial and error, ω_o is a constant to non-dimensionalize the rotational speed of the tool and R_s is the shoulder radius (refer to Figure 2.1).

Nandan et al. [28] defined the velocity at the tool pin interface in terms of the tool translation velocity and the tool pin angular velocity as follows:

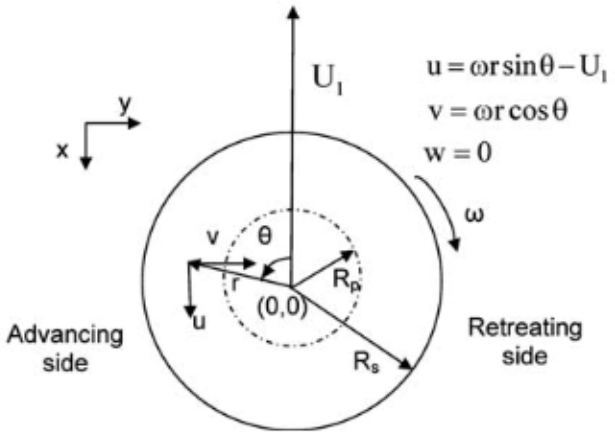

Figure 2.1 A top view for a schematic diagram of FSW tool [28].

$$u = (1-\delta)(\omega R_P \sin\theta - U_1) \tag{13}$$

$$v = (1-\delta)\omega R_P \cos\theta \tag{14}$$

At the shoulder interface, the velocity condition is expressed as follows:

$$\left.\begin{array}{l} u = (1-\delta)(\omega r \sin\theta - U_1) \\ v = (1-\delta)\omega r \cos\theta \end{array}\right\} in\ the\ range\ R_P \le r \le R_S \tag{15}$$

Equations (15) were implemented by Hasan et al. [42] and Pal et al. [30] using the commercial CFD code Fluent.

It can be concluded that in the Eulerian approach, it is very difficult to handle realistic frictional contact conditions. Several assumptions should be made to define the contact conditions and there is a lack of a unified description of the contact behavior.

The heat generated during FSW is due to plastic deformation and interfacial friction at the tool-workpiece interface. A steady-state energy conservation equation was used by Nandan et al. [28] and Pal et al [30] that has the following form:

$$\rho C_p \frac{\partial(u_i T)}{\partial x_i} = -\rho C_P U_1 \frac{\partial T}{\partial x_1} + \frac{\partial}{\partial x_i}\left(k \frac{\partial T}{\partial x_i}\right) + S_i + S_b \tag{16}$$

where C_p is the specific heat and k is the thermal conductivity of the workpiece/tool, S_i is the heat source term arising from friction at the tool workpiece interface, and S_b is the heat generation rate due to plastic deformation. The term S_i is represented as [25, 28]:

$$S_i = \left[(1-\delta)\eta\tau + \delta\mu_f P_N\right](\omega r - U_1 \sin\theta)\frac{A_r}{V} \tag{17}$$

where r is the radial center distance from the tool axis, V is the control volume enclosing any small area on the pin/workpiece interface (A_r), η is the mechanical efficiency, τ the maximum shear stress at yielding, μ_f is the spatially variable coefficient of friction, and P_N is the normal pressure.

Note that when full sticking conditions occur ($\delta = 0$), the heat is generated only by plastic deformation. However, when $\delta = 1$ heat is generated by friction. The heat generation rate due to plastic deformation is represented as $f_m\mu\phi$, where Φ is represented as follows:

$$\Phi = 2\left(\left(\frac{\partial u_1}{\partial x_1}\right)^2 + \left(\frac{\partial u_2}{\partial x_2}\right)^2 + \left(\frac{\partial u_3}{\partial x_3}\right)^2\right) + \left(\frac{\partial u_1}{\partial x_2} + \frac{\partial u_2}{\partial x_1}\right)^2 + \left(\frac{\partial u_1}{\partial x_3} + \frac{\partial u_3}{\partial x_1}\right)^2 + \left(\frac{\partial u_3}{\partial x_2} + \frac{\partial u_2}{\partial x_3}\right)^2 \tag{18}$$

where f_m is an arbitrary constant that indicates the extent of atomic mixing in the system. The value of f_m will tend to 1 for a well-mixed system in the atomic scale. In systems where the grains remain largely intact as in FSW [28], the value of f_m will be very small. Nandan et al. [28] and Cho et al. [25] assumed $f_m = 0.05$.

Pal et al. [30] defined the friction heat generation rate as:

$$\dot{q} = v_{slip}\, f_S = (v_{tool} - v_{mat})m\tau \tag{19}$$

where v_{slip} and f_S are the slip velocity and friction stress at the interface, v_{tool} and v_{mat} are the tangential velocity of tool and work- piece, τ is the shear yield stress of the workpiece and m is the friction factor.

Nassar and Khraisheh [29] defined the heat generation due to friction as follows:

$$q_{fr} = \mu\frac{F_{forge}}{A_{tool}}\omega r \tag{20}$$

where μ is the friction coefficient between the tool's shoulder and the workpiece, assumed in their work to be 0.3, r is the radial distance from the tool's axis, ω is the

rotational speed in rad/s, and $\frac{F_{forge}}{A_{tool}}$ is the normal pressure applied by the tool on the surface of the workpiece.

2.4. Results Based on Eulerian Approach

In this approach, most researchers studied temperature distribution, heat generation, and the flow of material. Zhang et al. [33] modeled FSW of the 6061-T6 aluminum alloy and conducted that high temperatures can be found at the interface and tend to decrease along the thickness direction. He also conducted that, the temperature values are higher in the advancing side than the retreating side as shown in Figure 2.2.

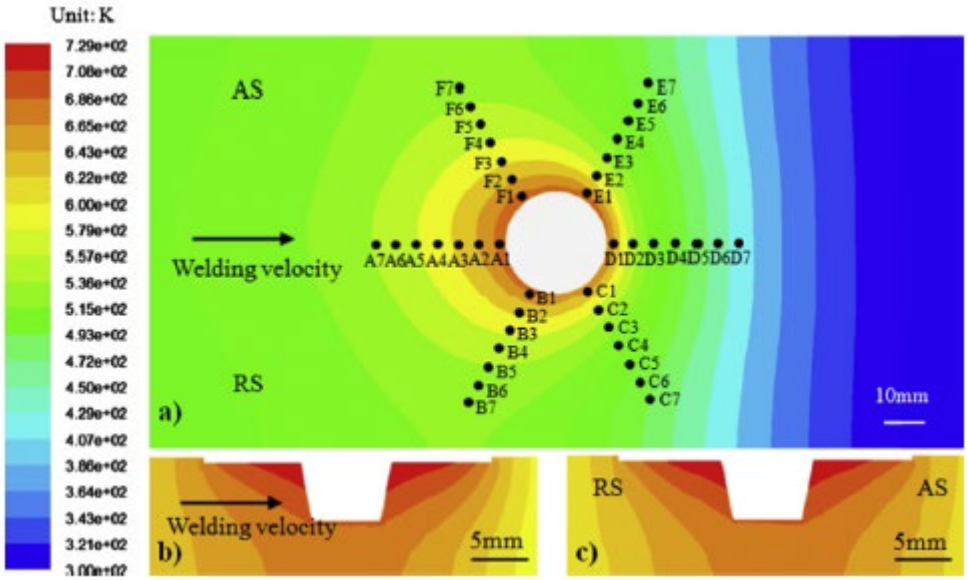

Figure 2.2 Temperature distribution in the workpiece: (a) Top view; (b) section view perpendicular to the welding direction; (c) section view parallels to the welding direction [33].

Cho et al. [25] used a 3D thermomechanical model simulating FSW to study heat transfer and material flow for ferritic stainless steel. They conducted that the major material transfer happens on the retreating side of the weld, which corresponds to a zero-velocity zone in the retreating side as shown in Figure 2.3.

Kim et al. [27] used a thermomechanical simulation of a friction stir butt welding process for AA5083-H18 to calculate streamlines near the tool with effective strain and temperature at different tool speeds and welding velocity as shown in Figure 2.5.

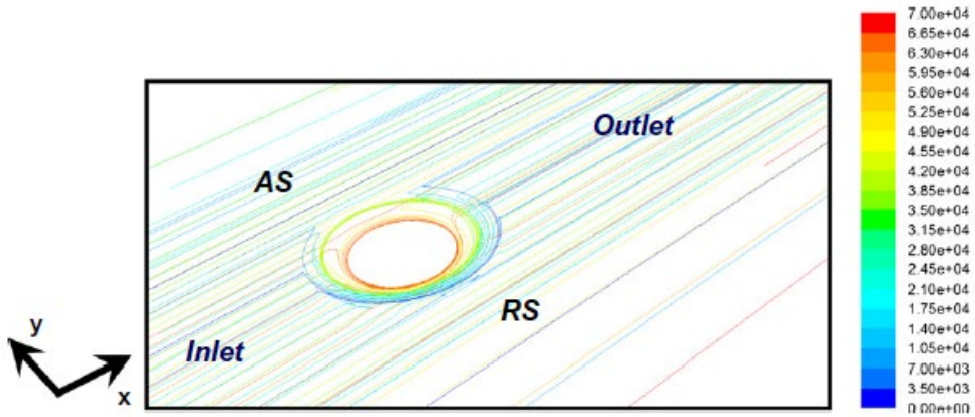

Figure 2.3 Flow streamlines around the tool [25].

Hasan et al. [42] studied the effect of viscous flow deformation around the tool on tool wear in FSW using a methodology based on a FLUENT CFD model and a modified Archard equation. The model displayed peak temperature results that are consistent with literature as shown in Figure 2.4.

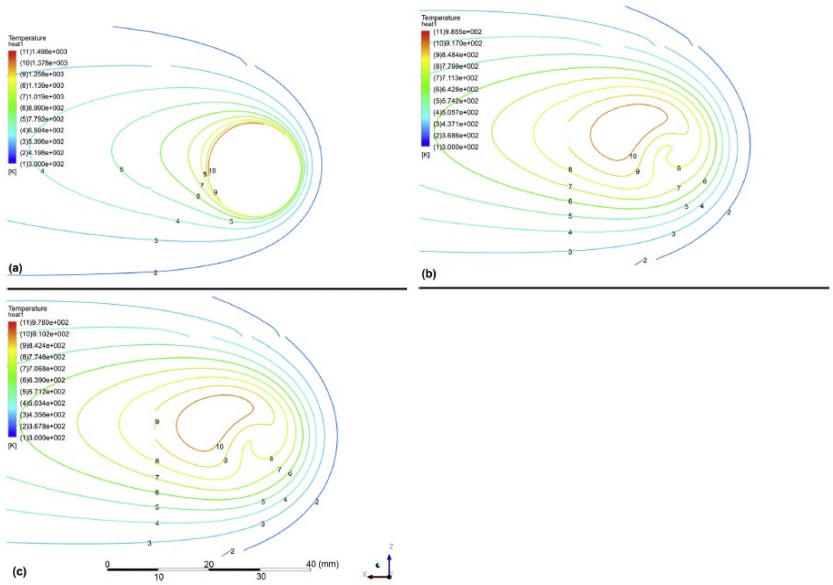

Figure 2.4 Temperature distribution at 0.002 mm weld distance:(a) plate to surface (b) pin tip plane (c) plate bottom surface [42].

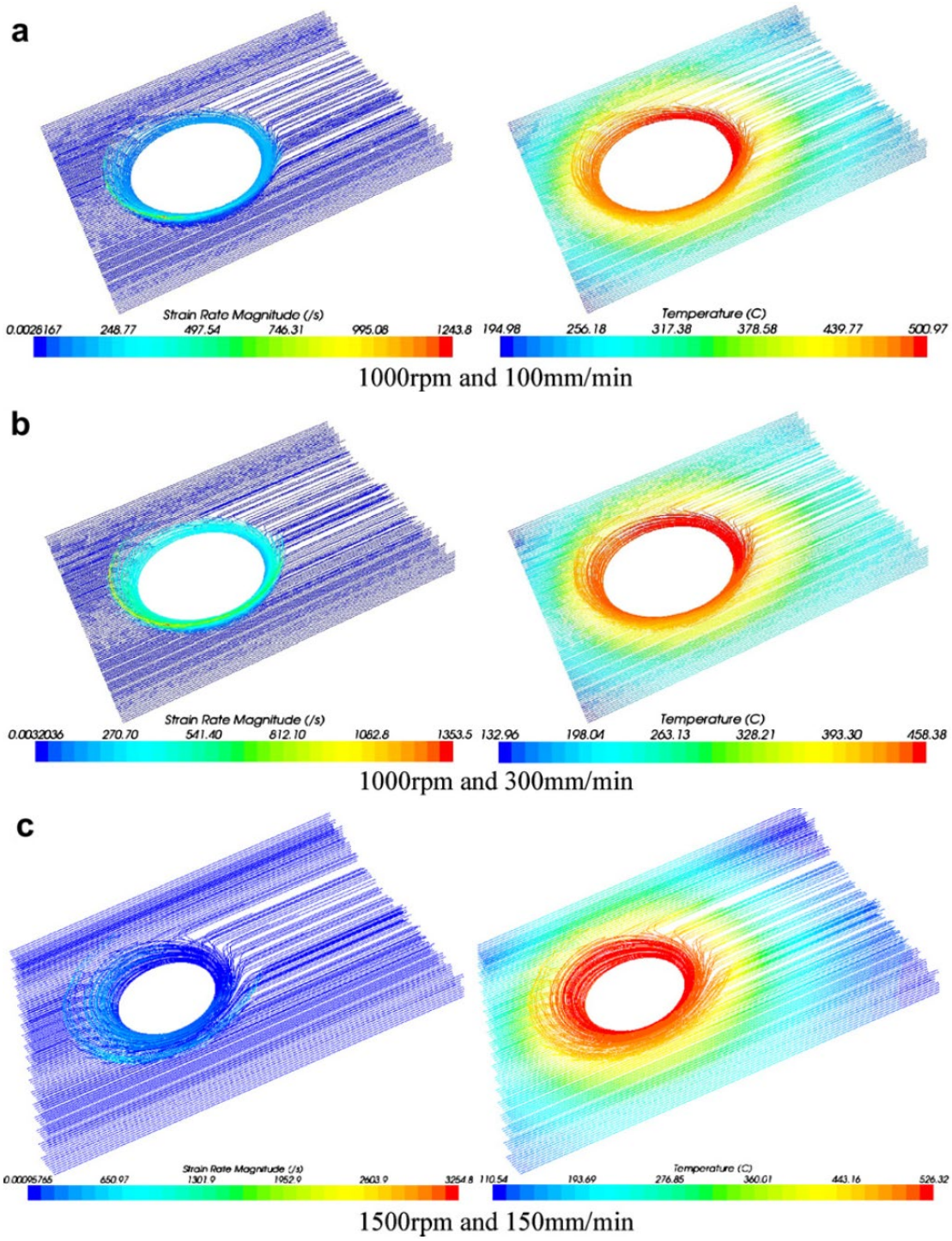

Figure 2.5 Streamlines with effective strain and temperature: (a) 1000 rpm and 100 mm/min; (b) 1000 rpm and 300 mm/min; (c) 1500 rpm and 150 mm/min [27].

Chapter 3. Lagrangian Approach

The Lagrangian description is a material description where the material domain $R_X \in R^{n_{sd}}$ with n_{sd} spatial dimensions, is made up of material particles X. This description is typically used in the computational solid mechanics; where the grid is attached to the material throughout the computational process. As each node in the grid follows the associated material particle, the grid deforms according to the relative movement of the connected nodes.

The advantages of Lagrangian grid-based methods include [23, 43]:

1- Free surfaces, moving boundaries and material interfaces can be easily tracked as grid nodes can be placed along boundaries and interfaces.
2- History-dependent field variables at any material point can be easily tracked and obtained because the material is attached to the grid.
3- Ability to handle arbitrary irregular geometries by using an irregular mesh.

Because of these advantages, Lagrangian methods are favored for solving computational solid mechanics problems. The main weakness of Lagrangian methods is their inability to handle large distortions of the computational domain without the need to rezone or re-mesh the computational domain; which is a time-consuming process.

In the Lagrangian approach, the material derivative reduces to a simple time derivative. This is because the material points and the grid points coincide during motion. The material derivative is defined as $\frac{D}{Dt} = \frac{\partial}{\partial t}\Big|_X$.

The governing conservation equations in PDE form in the spatial domain R_X consisting of material points X for the Lagrangian description are [23]:

$$\begin{aligned} &\text{Mass} && \frac{D\rho}{Dt} = \frac{\partial \rho}{\partial t}\Big|_X \\ &\text{Momentum} && \rho \frac{D\boldsymbol{v}}{Dt} = \rho \frac{\partial v}{\partial t}\Big|_X \\ &\text{Energy} && \rho \frac{DE}{Dt} = \rho \frac{\partial E}{\partial t}\Big|_X \end{aligned} \quad |(21)$$

The spatial gradient for Lagrangian description is:

$$\boldsymbol{\nabla_x = F^{-T}.\nabla_X}$$

where $\boldsymbol{F = \frac{\partial x(X,t)}{\partial X}}$ is the deformation gradient accounting for grid deformation, $\boldsymbol{\nabla_X}$ is the material gradient calculated at the original position of the mesh.

A number of studies [10, 14, 44-49] have been performed to model the FSW process using pure Lagrangian approach. However, the severe deformation during FSW causes high distortion of the mesh that has an adverse effect on the accuracy of the results. For example, Khandkar et al. [46] simulated FSW using DEFORM-3D in order to assess the residual thermal stresses that develop during the welding process. They reported that most experimental stress values found in the literature are much lower than the values calculated by their model. They indicated that this discrepancy is because the finite element meshes need to be adaptive in nature to better simulate the residual stresses.

To avoid the disadvantages of the pure Lagrangian description, several researchers used the Arbitrary Lagrangian-Eulerian (ALE) description that combines the best features of Eulerian and Lagrangian descriptions. In ALE, the mesh moves independently of the material so that mesh distortion is minimized. The nodes of the computational mesh may be held fixed (Eulerian description), moved with the continuum (pure Lagrangian description), or moved to in an arbitrarily specified more advantageous way. This freedom of movement improves the ability of the mesh to handle large distortion of the continuum without affecting the accuracy of the analysis.

In ALE, a referential domain Rχ is used; where χ represents the reference coordinates that identify the grid points. The grid velocity is introduced as follows:

$$\hat{v}(\chi, t) = \left.\frac{\partial x}{\partial t}\right|_{\chi} \tag{22}$$

The convective velocity *c*, which is the relative velocity between the material and the mesh is defined as:

$$c := v - \hat{v} \tag{23}$$

To apply the conservation laws in the ALE referential frame, the material derivative is defined as follows:

$$\frac{D}{Dt} = \frac{\partial}{\partial t}\Big|_{\chi} + \boldsymbol{c}.\boldsymbol{\nabla}_{\boldsymbol{x}} \tag{24}$$

If the material velocity in above equation is replaced by the convective velocity, the ALE governing conservation equations in PDE form is obtained:

$$\begin{aligned} &\text{Mass} && \frac{\partial \rho}{\partial t}\Big|_{\chi} + \boldsymbol{c}.\boldsymbol{\nabla}_{\boldsymbol{\chi}}\rho = -\rho\boldsymbol{\nabla}_{\boldsymbol{\chi}}.\boldsymbol{v} \\ &\text{Momentum} && \rho\left(\frac{\partial v}{\partial t}\Big|_{\chi} + (\boldsymbol{v}.\boldsymbol{\nabla}_{\boldsymbol{\chi}})\boldsymbol{v}\right) = \boldsymbol{\nabla}_{\boldsymbol{\chi}}.\boldsymbol{\sigma} + \rho\boldsymbol{b} \\ &\text{Energy} && \rho\left(\frac{\partial E}{\partial t}\Big|_{\chi} + \boldsymbol{v}.\boldsymbol{\nabla}_{\boldsymbol{\chi}}\boldsymbol{E}\right) = \boldsymbol{\nabla}_{\boldsymbol{\chi}}.(\boldsymbol{\sigma}.\boldsymbol{v}) + \boldsymbol{v}.\rho\boldsymbol{b} \end{aligned} \tag{25}$$

ALE technique has the ability to implement sliding boundary conditions in the interface between the tool and the workpiece by assuming a constant slip rate or various values for the coefficient of friction. However, as the ALE uses Lagrangian elements, it cannot withstand voids and need to be filled continuously with the material. As a result, severe mesh distortions will happen to lead to failing the model for a non-converge solution.

Another method that was used to solve the issue of mesh distortion is the coupled Eulerian-Lagrangian (CEL) method. The CEL method suggested by Noh W.F. [50] combines the advantages of both Lagrangian and Eulerian methods. It engages them in separate regions (or with some overlap) of the problem domain. Therefore, the CEL method has the ability to simulate material flow and void formation during the FSW process. Usually, the practice is to discretize solid materials in Lagrangian frame and fluids or material that behave like fluids in a Eulerian frame. Both grids interact with each other through a coupling module in which an exchange of computational information is occurred by mapping or other interface treatment.

According to Xiamen [51], the governing equations of the CEL technique can be written as in Equations (26), (27), and (28).

Continuity equations:

$$\frac{D\rho}{Dt} + \rho\nabla.v = \frac{\delta\rho}{\delta t} + v.\nabla\rho + \rho\nabla.v \tag{26}$$

Momentum Equation:

$$\rho.\frac{Dv}{Dt} = \nabla.\sigma + \rho b \tag{27}$$

$$\frac{D(v)}{Dt} = \frac{\delta(v)}{\delta t} + v.\nabla(v)$$

Energy equations:

$$\rho \frac{DE}{Dt} = \sigma.\dot{\varepsilon} + \rho\dot{Q} \tag{28}$$

where $\dot{\varepsilon} = 1/2(\nabla v + \nabla v^T)$ is strain tensor ratio.

The boundary of the Lagrangian domain is taken to represent the interface between the different domains. The velocity of the Lagrangian boundary is used as a kinematic constraint in the Eulerian calculation, while the stress from the Eulerian cell is used to calculate the resulting surface stress on the Lagrangian domain [52]. Various CEL algorithms may be classified depending on how they treat the interface condition.

The common practice when using CEL technique to model FSW is to discretize the tool using the Lagrangian frame and the workpiece using Eulerian frame [53-55]. As the CEL method discretizes the workpiece using a Eulerian frame, it was used to simulate material mixing as well as plunge and dwell phases of FSW [53, 55]. It was used also by Al-Badour et al. [53] to study void formation.

3.1. Material Constitutive Model

The commonly used constitutive models in simulation of FSW/FSP using Lagrangian approach are the Johnson-Cook's model, the Sellars and Tegart model, and the Zerilli-Armstrong model. Those material models shall be discussed in details in this section.

3.1.1. Johnson-cook model. Johnson-Cook model is widely used for modeling of FSW/FSP process [53-56]. That is due to its ability to describe the behavior of the material when subjected to large strain, high deformation, and high-temperature conditions. JC model defines the yield stress as a function of the equivalent plastic strain, the equivalent plastic strain rate, and temperature using the following empirical relation:

$$\sigma_y\left(\varepsilon_p, \dot{\varepsilon_p}, T\right) = \left[A + B(\varepsilon_p)^n\right]\left[1 + Cln(\dot{\varepsilon_p^*})\right][1 - (T_h)^m] \tag{29}$$

where σ_y is the flow stress, T_h is the homologous temperature, and $\varepsilon_p, \dot{\varepsilon_p}$ are the equivalent plastic strain and the equivalent plastic strain rate respectively. *A, B, C, n*, and *m* are the material constants.

$$\dot{\varepsilon_p}^* := \frac{\dot{\varepsilon_p}}{\dot{\varepsilon}_{p0}} \text{ and } T_h := \frac{(T - T_0)}{(T_m - T_0)} \tag{30}$$

where $\dot{\varepsilon}_{p0}$ is a user-defined plastic strain-rate, T_0 is a reference temperature (room temperature), and T_m is a reference melting temperature. When we have $T_h < 0$, then we assume that $m = 0$.

Grujicic et al. [57] listed a number of shortcomings of this model that are mainly related to microstructural changes during FSW. These shortcomings are due to the inability of this model to account for the following aspects:

- The irreversible decrease in dislocation density due to annealing and recrystallization.
- Grain growth due to high-temperature exposure.
- Dynamic recrystallization induced grain refinement.

As parameter *A* is affected by the grain size, in case plastic deformation takes place at a temperature that is below the recrystallization temperature, the value of *A* would remain constant. However, the effects of dynamic recrystallization induced grain refinement and grain growth should be accounted for in case the deformation temperature exceeds the recrystallization temperature. As a result, Grujicic et al. [57] calculated the parameter *A* based on the Hall-Pitch equation:

$$A = A_{HP} + K_{HP} D^{-1/2} \tag{31}$$

where A_{HP} is the single crystal annealed yield strength, K_{HP} is an alloy-specific grain size invariant parameter, and *D* is the mean grain size. The mean grain size equation has the following form [57]:

$$D(t + \Delta t) = D(t) + \dot{D}_{coarsening}\Delta t + \dot{D}_{refinement}\Delta \mathrm{t} \tag{32}$$

where $\dot{D}_{coarsening}$ is the grain size growth rate due to Oswald ripening, and $\dot{\boldsymbol{D}}_{\boldsymbol{refinement}}$ is the grain size refinement rate due to dynamic recrystallization. The grain growth is assumed to be inversely proportional to the grain size as follows:

$$\dot{D}_{coarsening} = \frac{k_{coarsening}}{D} \tag{33}$$

where $k_{coarsening}$ is a parameter that depends on temperature as follows:

$$k_{coarsening} = k_{coarsening,0} \exp(\frac{-Q_{coarsening}}{RT}) \tag{34}$$

where $k_{coarsening}$ is the pre-exponential rate term, R is the universal gas constant, and T is the absolute temperature. The grain refinement rate is relatively proportional to the recrystallized plastic strain as follows:

$$\dot{D}_{refinement} = D_{refinement} \frac{\Delta\bar{\varepsilon}^{pl}_{recrystallized}}{\Delta t} \tag{35}$$

where $D_{refinrment}$ is taken as a constant evaluated from experiments and The recrystallized equivalent plastic strain increment, $\Delta\bar{\varepsilon}^{pl}_{recrystallized}$, is calculated as follows:

$$\Delta\bar{\varepsilon}^{pl}_{recrystallized} = (\dot{\bar{\varepsilon}}^{pl}_{recrystallized}\left(\bar{\varepsilon}^{pl}_{recrystallized}\right)^{p} \exp(\frac{-Q_{recrystallized}}{RT})\Delta t \tag{36}$$

where $\dot{\bar{\varepsilon}}^{pl}_{recrystallized}$ is a pre-exponential rate, p is a constant, and $-Q_{recrystallized}$ is the associated recrystallization energy. The values of these parameters are determined from experiments using an inverse engineering approach.

Grujicic et al introduced a modified equivalent plastic strain that accounts for recrystallization, $\Delta\bar{\varepsilon}^{pl}_{modified}$, to replace the equivalent plastic strain, ε_p. The modified equivalent plastic strain has the following incremental form:

$$\bar{\varepsilon}^{pl}_{mod}(t + \Delta t) = \bar{\varepsilon}^{pl}(t) + \Delta\bar{\varepsilon}^{pl} + \Delta\bar{\varepsilon}^{pl}_{recrystallized} \tag{37}$$

Grujicic et al.[57] implemented the modified JC model in Abaqus to predict the grain size and the mechanical properties at room temperature in different FSW zones. They reported that the implementation of the modified JC model in computational analysis codes can be used to establish processing/microstructure and property relations in the weld that could serve as a guide in the selection of the optimum welding process parameters.

Table 3.1 Modified Johnson-Cook material parameters for AA5083

Parameter	Symbol	Unit	Value	Ref.
Reference Strength	A	MPa	167	[56]
Strain Hardening Parameter	B	MPa	596	[56]
Stain Hardening exponent	n	N/A	0.551	[56]
Room Temperature	T_{room}	K	293	[56]
Strain-rate coefficient	C	N/A	0.001	[56]
Melting Temperature	T_{melt}	K	893	[56]
Temperature Exponent	m	N/A	1	[56]
Alloy-specific Grain size invariant parameter	K_{HP}	MPa.μm$^{1/2}$	827	[57]
Pre-exponential rate term	$k_{coarsening,o}$	μm^2/s	31.59	[57]
Activation Energy	$Q_{coarsening}$	KJ/mol	23.75	[57]
Single Crystal annealed yield strength	A_{HP}	MPa	50	[57]

3.1.2. Sellars and Tegart model. Another constitutive model that is used often in simulating FSW is the one proposed by Sellars and Tegart [35], which relates the flow stress to temperature and strain rate as follows:

$$\sigma_e = \sigma_R sinh^{-1}\left[(\frac{Z}{\beta})^{1/m}\right] \tag{38}$$

where σ_R, β, m are material constants. Z is the Zener-Hollomon parameter, defined as:

$$Z = \dot{\varepsilon}_e \exp(\frac{Q}{RT}) \tag{39}$$

where Q is the activation energy of the material, and R is the universal gas constant.

Sellars and Tegart model assumes that the flow stress is independent of the plastic strain and equal to the dynamic recrystallization steady state stress. In other words, it assumes stress saturation at a constant strain rate, which might be the case for high deformation processes. On the other hand, it might neglect and overestimate stresses at low strains [36]. Moreover, Sellars and Tegart model can predict grain size, as the Zener Hollomon parameter is related directly to the average grain size of dynamic recrystallization [37]. It has been used by Pan et al. [17] with SPH numerical method to study temperature variation, grain size and micro-hardness, and texture evolution. Also, it was used by Nassar and Khraisheh [29] with CFD analysis to study temperature

distribution, partial melting and effect of partial melting on heat evolution and material flow.

The Sellars and Tegart model reduce the computational time as it assumes stress saturation. On the other hand, it does not describe strain hardening, the high-temperature effect on grain growth, and dynamic recrystallization induced softening phenomenon.

3.1.3. Zerilli- Armstrong model- ZA6. The Zerilli-Armstrong model is based on thermally activated dislocation mechanics [58]. Since it is based on dislocation interactions, it has different forms for different material type structures (BCC, FCC, and HCP).

For FCC metals, the dislocation motion is restricted by dislocation-dislocation interactions, which leads to considerable strain hardening [59]. The general form that developed by Zerilli and Armstrong for FCC metals is as follows [58]:

$$\sigma = C_0 + C_1\varepsilon^{1/2}\exp(-C_2T + C_3Tln\dot{\varepsilon}) + K\varepsilon^n \tag{40}$$

The relation shows dependencies of temperature softening and strain rate sensitivity on strain hardening. While for bcc metals, the dislocation motion is controlled by the Peierls-Nabarro stress stemming from the dislocation –lattice interaction, which results in slight strain hardening [59]. The general form that developed by Zerilli and Armstrong for bcc structure is as follows [58]:

$$\sigma = C_0 + Bexp(-C_2T + C_3Tln\dot{\varepsilon}) + K\varepsilon^n \tag{41}$$

The strain hardening is decoupled from strain rate sensitivity and temperature softening, and a strain hardening term is added. Generally, the temperature softening, strain rate sensitivity and grain size dependencies are larger if compared with fcc metals [57]. The hcp metals, have a behavior that is between the FCC and BCC metals. The ZA model is able to describe the strain rate, strain hardening, temperature softening, and grain size.

The Zerilli and Armstrong model was used extensively to simulate high temperature and high strain rate problems [60-62]. Although it was rarely used in modeling of FSW, it was recommended by Ammouri and Hamade for modeling of FSP of twin roll cast AZ31B [36]. The Zerilli and Armstrong model cost less

computationally than Jonson-Cook model, but it does not consider grain growth due to high temperature.

3.2. Friction Model

In this section, the friction models that are commonly used in modeling friction within the FSW process are addressed. Also, the contact conditions shall be discussed.

There are two main advantages of using physical based contact models to describe the contact conditions (sticking, sliding, partial sticking/sliding) at the tool material interface. The first advantage is that void formation can be predicted if the material constitutive model accounts for elastic behavior (compressibility) since material contact is not enforced in the analysis. The second advantage is that the mechanical interaction between the tool and workpiece can be determined using numerical simulations. Based on simulation results, the heat generated by friction can be calculated without the need for using analytical models similar to the ones used in CFD based simulations. In this section, two friction models that are commonly used in literature will be described.

3.2.1. Modified coulomb friction law. In the classical Coulomb model, the contact pressure between the two parts in contact is directly related to the frictional shear stress. In the classical model, the frictional shear stress is calculated as follows:

$$\tau_f = \mu p \tag{42}$$

where μ is the coefficient of friction which plays a key role in shear stresses transmission, p is the contact pressure, and τ_f is the frictional shear stress. As the relation between τ_f and p is linear, at high contact pressures τ_f may exceed the shear strength of the material. Thus, the Coulomb model was modified to define the frictional shear stress as the minimum of the classical coulomb and the material critical shear stress of the softer material in contact as follows:

$$\tau_f = \min(\mu p, \frac{\sigma_u}{\sqrt{3}}) \tag{43}$$

where μ is the coefficient of friction, p is the contact pressure, σ_u is the ultimate tensile strength., and $\frac{\sigma_u}{\sqrt{3}}$ is the shear strength of the material.

Several researchers have used the modified Coulomb friction model in modeling FSW [11, 56, 63-65]. This model is a combination of the classical Coulomb model that is appropriate to describe friction between rigid bodies in sliding contact and the Tresca model that limits frictional shear stress by the maximum shear admissible by the material. Zhang et al. [63] compared between the classical and modified Coulomb in the simulation of friction stir welding, and he conducted that the classical model fails to simulate temperature distribution and material flow at higher angular velocities due to the dynamic effect of the tool at higher velocities.

Several values for the coefficient of friction were suggested in the literature. Shmidt and Hattel [66] used a value of $\mu = 0.3$ between the AA 2024-T3 workpiece and the tool. Hamilton et al. [67] assumed that the coefficient of friction varies between 0.4 and 0.5 depending on the energy generation level. As the energy generated increases, the workpiece material softens causing the tool to slip, which lowers the friction coefficient.

On the other hand, Song et al. [68] suggested that the coefficient of friction be linearly temperature dependent, given by:

$$\mu = -0.00027T + 0.5810 \tag{44}$$

where T is the local temperature at the tool surface.

3.2.2. The viscoplastic friction law. Assidi et al. [64], Chiumenti et al. [24], and Guerdoux and Fourment [69] used the Norton's model that takes into account the surface temperature and the sliding velocity. Norton's model has the following form:

$$\tau_f = -\alpha_f K(T) \|\Delta v_s\|^{q-1} \Delta v_s \tag{45}$$

where α_f and q are the Norton friction coefficients, Δv_s is the relative sliding velocity, and $K(T)$ is the temperature dependent material consistency. Assidi et al. [64] calibrated this model for an AA6061 aluminum plate and an unthreaded concave tool by comparing the welding forces and tool temperature obtained from simulations to experiments at different tool travel speeds. A good agreement was obtained for the welding forces. However, the tool temperature was not predicted accurately. The highest values for temperature were obtained experimentally at the tool probe. However, the model predicts the highest temperature at the tool shoulder.

3.3. Heat Generation

Though some researchers used analytical models with FEM to predict heat generation due to friction [10, 67, 68], it is believed that a physical based model is more appropriate for heat generation modeling as it can be implemented for any type of tools and workpiece materials. When the workpiece is treated as elastic/plastic material, the heat generated due to friction can be represented as follows [70]:

$$q_{surf} = \mu p \dot{\gamma} \tag{46}$$

where μ is the friction coefficient, p the pressure and $\dot{\gamma}$ is the slip rate.

The heat generated due to plastic deformation can be represented as follows [70]:

$$\eta s_{ij} \dot{\varepsilon}_{ij}^{pl} \tag{47}$$

where η the fraction of plastic energy dissipation, s_{ij} the deviatoric stress tensor and $\dot{\varepsilon}_{ij}^{pl}$ is the plastic strain rate tensor.

Chapter 4. Mesh Free Methods

A meshfree method is defined as a method that establishes a system of algebraic equations for all the problem domain without using mesh to discretize the domain [71].

Generally, meshfree methods use a set of particles or distributed nodes without mesh as the connection between them, but rather depend on their interaction with the adjacent particles, in order to provide accurate and stable numerical solution for integral equations or PDEs with all possible boundary conditions. Meshfree methods were developed mainly to apply it on the problems which conventional FDM and FEM are difficult to apply; like problems with deformable boundary, moving interface (for FDM), free surface, large deformation (for FEM), complex mesh generation, mesh adaptivity, and multi-scale resolution.

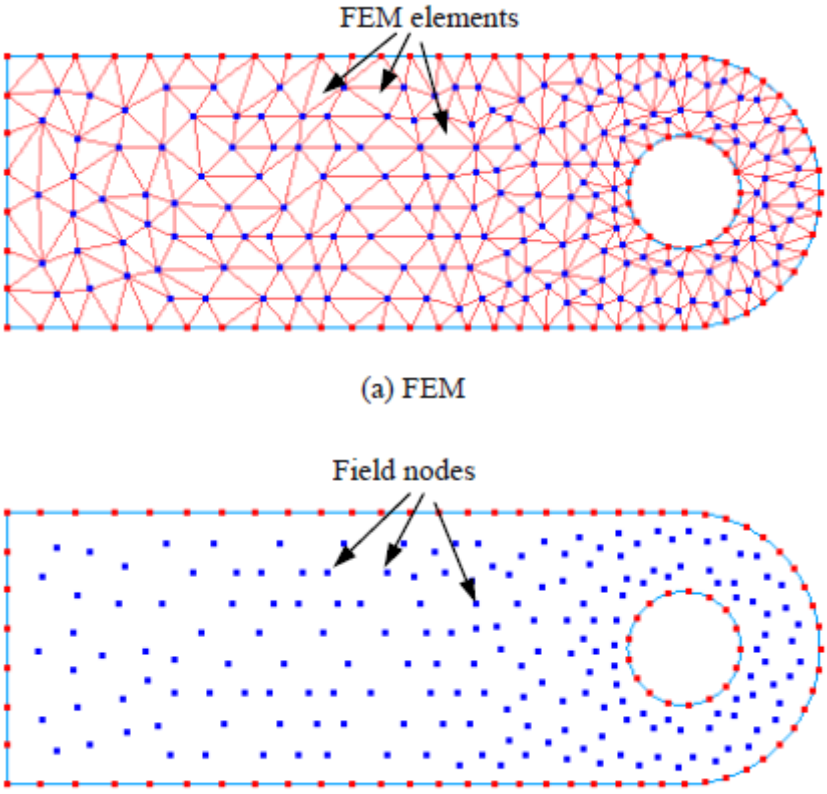

Figure 4.1 FEM domain and Mesh free method domain

All the meshfree methods share common features, but they differ from each other in the ways of function approximation and the implementation process.

Meshfree methods were used to solve both problems of solid mechanics and fluid dynamics. In this section, the meshfree methods used to simulate FSW shall be investigated and described whether considering the fluid approach or the solid approach in describing the FSW problem.

4.1 Meshfree Methods for Fluid Approach

The meshfree methods are considered a promising option to be used in solving CFD problems. Basically, there are three types of methods that are utilized in solving CFD problems [71]:

1. Finite integral representation methods (smoothed particle hydrodynamics method (SPH), and reproducing kernel particle method (RKPM)).
2. Finite series representation methods (meshless Petrov-Galerkin method (MLPG), and the local radial point interpolation method (LRPIM)).
3. Finite differential representation methods (the finite point method, and the finite difference method with arbitrary irregular grids).

In this section, only the SPH method shall be explored as it is the most popular in solving FSW problem.

4.1.1. Smoothed particles hydrodynamics method. Smoothed particle hydrodynamics (SPH) method was developed by Lucy [72] as a meshfree and particle method for modeling astrophysical phenomena without boundaries. SPH is basically a Lagrangian particle code without a background spatial mesh which it can take excessive deformation in an original Lagrangian frame [73]. The method was developed for hydrodynamic problems that in the form of PDE equations of field variables. Attempts have been made to search for numerical solutions since it is not usually possible to find an analytical solution. The steps to obtain a numerical solution are as follows: first, discretizing the problem domain where the PDEs are interpreted. Second, a method should be used to yield an approximation to the field function values and their derivatives at any point. Then, a set of ODEs (in a discretized form with respect only to time) should be produced by applying the function approximation to the PDEs. At last, these ODEs should be solved using conventional finite difference method.

As mentioned above, there should be a method to provide an approximation to the PDEs. The method that is used for SPH is the integral function representation method or termed as Kernel approximation of field functions. Furthermore, the Kernel approximation is also approximated further using the so-called particle approximation.

Generally, the particle approximation method replaces the integration in the kernel of the field function and its derivatives with summation over all the corresponding values at the neighboring particles in a local domain called the support domain. In this section, only the implementation of SPH in solving Navier-Stokes equations for CFD problems is discussed.

The mass, momentum, and energy equations with SPH discretization is written as follows [17]:

$$\frac{d\rho_i}{dt} = \rho_i \sum_j \frac{m_j}{\rho_j} v_{ij}.\nabla_i W(r_i - r_j, \bar{h}_{ij}),$$

Mass

$$\frac{dv_i}{dt} = -\sum_j m_j \left(\frac{P_i + P_j}{\rho_i \rho_j} + \sqcap_{ij}\right) \nabla_i W(r_i - r_j, \bar{h}_{ij}) + F_i^b,$$

Momentum

Energy

$$C_{p,i}\frac{dT_i}{dt} = -\sum_j \frac{m_j}{\rho_i \rho_j}\frac{4k_i k_j}{k_i + k_j}(T_i - T_j)\,\frac{r_{ij}.\nabla_i W(r_i - r_j, \bar{h}_{ij})}{|r_{ij}|^2} - \frac{1}{2}\sum_{jj} m_j \sqcap_{ij} v_{ij}.\nabla_i W(r_i - r_j, \bar{h}_{ij}) - RT_i\delta_i \quad (48)$$

where $\sqcap_{ij}$ is the viscous term expressed as follows:

$$\sqcap_{ij} = -16\,\frac{b v_{ij}.r_{ij}}{|r_{ij}|}\frac{\mu_i \mu_j}{(\mu_{i+}\mu_j)h\rho_i\rho_j} \quad (49)$$

where $i\ and\ j$ denote the neighbor fluid particles, r is the position, v is particle velocity, and μ is the fluid viscosity.

The strategy of the formulation of SPH method led it to be a meshfree, adaptive, stable and Lagrangian solver for dynamic problems [43] as discussed below.

- The SPH is a meshfree method since the domain is represented by particles which are not connected with any mesh.
- The SPH method can handle severe deformation problems (adaptive) since the particle approximation that applied every time step depends only on the current local distribution of the particles.

- The SPH method can have all the features of the Lagrangian method since the particle approximations are applied to all terms related to field functions in the PDEs to obtain a set of ODEs in discretized form with respect to time only.
- The SPH method can solve dynamic problems, since an explicit integration algorithm is used to solve the ODEs, in order to achieve fast time stepping and to determine the time history of all the field variables for the whole particles.
- In the SPH method, complex constitutive behavior can be applied simply and accurately.

On the other hand, SPH formulation has key limitations summarized as follows:

- In solid applications, SPH formulation has difficulties associated with the tensile instability and the spurious modes.
- As the SPH formulation has an explicit dynamic nature, it prevents the adoption of an implicit version for the post-welding residual stress analysis.

Pan et al. [17] simulated FSW and considered the welded material as a non-Newtonian fluid. They used the above formulation of SPH based on Navier-Stokes equations to study how the tool speed and rotational speed can affect grain size and temperature distribution, material hardness, and texture in the welding zone.

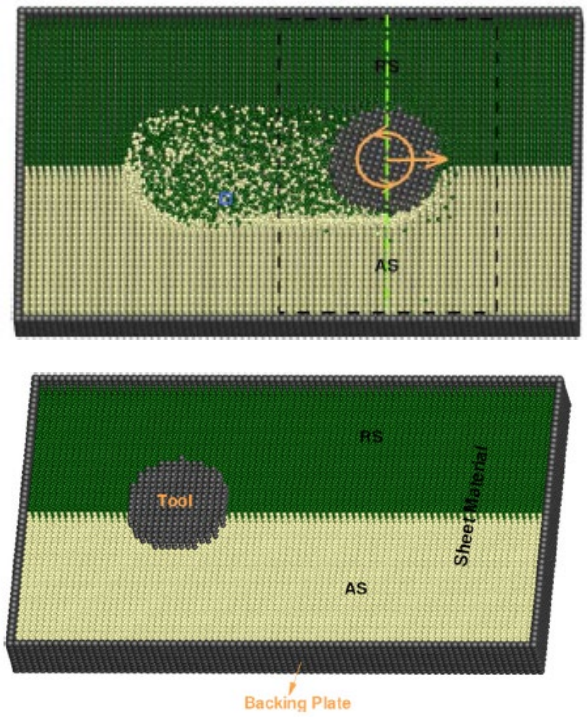

Figure 4.2 3D SPH model for FSW [15]

4.2. Meshfree Methods for Solid Approach

There are many meshfree methods that can be used to solve solid mechanics problems, but the most popular ones are the element-free Galerkin method (EFG) developed by Belytschko et al. [74] and the meshless local Petrov-Galerkin method (MLPG) developed by Atluri and Zhu (1998). In this research, only the EFG method will be explored as it was used to model FSW.

4.2.1. Element –free Galerkin method. The Element-Free Galerkin method (EFG) was developed by Belytschko et al. [74], which is basically a Galerkin weak form with Moving Least Squares Approximation. The spark of the development of EFG was the raising of the Diffuse Element Method (DEM) by Nayroles et al. [75]. The combination of the interpolants that Nayroles et al. [75] used in their method (which later called Moving Least Squares interpolants (MLS)) with the Galerkin method created the EFG [74]. The discretized systems of the equation based on the weak form is considered more stable and offers more accuracy than the one based on the strong form. Also, the MLS offers a smooth and continuous approximated field in the problem domain. One drawback of the MLS shape functions that it does not possess the Kronecker delta function property, which allows ease in treating boundary conditions as same as in FEM.

The interesting feature of EFG is its adaptivity; because it does not need a new finite element mesh to adopt an incremental variation in the number of points in the component, nevertheless it does need a background mesh for integration of system matrices.

In the solution procedure of EFG method, first, the geometry of the problem domain is modeled. Then, the problem domain is represented by a set of nodes as in Figure 4.3. Next, the assembly of system matrices is done in two loops; one outer loop for the cells of the background mesh, and one inner loop for the Gauss quadrature points within a cell [71].

According to Simkins and Li [76], meshfree methods based on Galerkin approach are very effective in dealing with von Mises and pressure dependent materials in large deformation analysis. Wu et al. [19] introduced a numerical procedure based on the EFG method, which uses the Lagrangian meshfree convex approximation and two-way adaptive procedure for the thermomechanical analysis of the FSW process. They founded that, the Lagrangian meshfree convex approximation has a vital role in

suppressing tensile instability, minimizing the adaptivity-induced discretization sensitivity, simplifying the boundary condition enforcement as it allows weak Kronecker Delta property at the boundaries, and offering a precise and reliable projection operation in the remapping procedure. For more details about the EFG method formulation in FSW, you can refer to the work done by Wu et al. [19].

Major advantages of this method include: first, no post-processing is needed for the field variables, which are derivatives of primary-dependent variables. Second, it has a great capability in industrial applications, since meshing nodes and elements are not needed here. Last, it is considered an adaptive method.

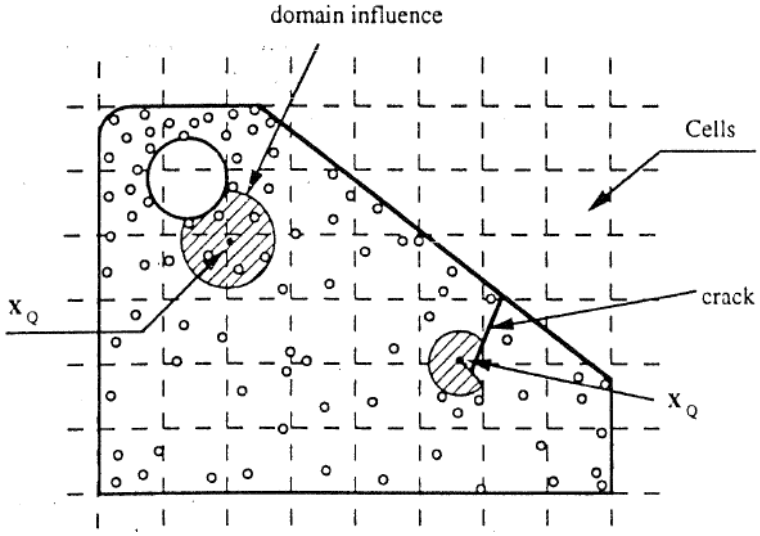

Figure 4.3 Cell Structure for Quadrature in EFGM and domains of quadrature point [46].

Chapter 5. Numerical Modeling of Submerged Friction Stir Welding

5.1 Introduction

Submerged friction stir welding (SFSW) or also called underwater friction stir welding (UFSW), is a process of choice to potentially improve the FSW process. In SFSW, water is used as a coolant to reduce peak temperatures and increase the cooling rate at the weld zone. The reason behind using a coolant is to limit grain growth in FSW due to high temperatures induced, which leads to the reduced mechanical performance of the weld joint [77-79].

SFSW enhances the mechanical properties of the material by reducing welding defects such as shrinkage, porosity, and solidification cracking. Moreover, SFSW produces a high-quality weld joint, due to the distinct change in grain size in various zones of the joint. Also, due to the high heat capacity of water, the width of TMAZ and HAZ regions is reduced by minimizing the heat input due to friction and plastic deformation [80, 81]. The SFSW process is commonly used for Aluminum alloys, as it is adequate for responsive alloys to high temperatures amid the welding process [82]. SFSW has a wide range of applications such as oil and fuel tanks, shipbuilding, and submarines.

In this section, a 3D coupled thermo-mechanical finite element model was developed in ABAQUS Explicit software to simulate the FSW/SFSW processes by using the coupled Eulerian-Lagrangian (CEL) approach.

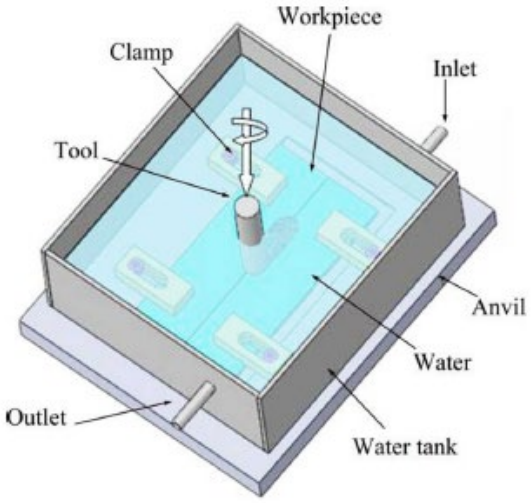

Figure 5.1 Sketch of SFSW [83]

5.2. Experimental Procedure

The developed model is based on the experimental investigation of underwater friction stir welding done by Kishta and Darras [22]. The material is Aluminum alloy 5083 marine-grade of 4 mm thickness sheet. A tool with a flat shoulder of 15mm diameter, a threaded pin of 5 mm diameter and 4 mm length was used in the experiment. Different rotational speeds in a range of 1000 rpm – 1700 rpm and a welding speed of 75 mm/min are considered. A detailed description of the experiment can be found in the investigation held by Kishta and Darras [22].

5.3. Model Description

A 3D coupled thermo-mechanical model was established to predict temperature distribution during FSW/SFSW processes, based on CEL technique, modified Coulomb's frictional law, and Johnson-Cook constitutive material law. A detailed description of the model is presented in this section.

5.3.1. CEL model. In the CEL method, the workpiece was modeled as a Eulerian part, while the tool was modeled as a Lagrangian part. The conservation equations in the Eulerian formulation are written using the spatial time derivative, while in the Lagrangian formulation the material time derivative is used. The relation between the above derivatives is as follows [84]:

$$\frac{D\varphi}{Dt} = \frac{\partial\varphi}{\partial t} + v.(\nabla\varphi), \tag{50}$$

where v is the material velocity, φ is an arbitrary solution variable, $\frac{D\varphi}{Dt}$ is the material time derivative, and $\frac{\partial\varphi}{\partial t}$ is the spatial time derivative.

Then, the Lagrangian mass, momentum and energy equations represented in the Eulerian conservation equations are as follows:

$$\begin{aligned} &\text{Mass} && \frac{\partial\rho}{\partial t} + \nabla.(\rho v) = 0, \\ &\text{Momentum} && \frac{\partial\rho v}{\partial t} + \nabla.(\rho v \otimes v) = \nabla.\sigma + \rho b, \\ &\text{Energy} && \frac{\partial e}{\partial t} + \nabla.(ev) = \sigma : D, \end{aligned} \tag{51}$$

5.3.1.1 ***Geometrical model and mesh generation.*** To solve the governing equations for the FSW process, ABAQUS Explicit was used. For the sake of computational time reduction, only a localized region of the workpiece is considered in the analysis. The workpiece thickness is 4 mm, while the Eulerian domain is 6 mm thickness. The size of the tool pin is 5 mm diameter and 3 mm length, with a flat tool shoulder of 15 mm diameter. The Eulerian domain was meshed using 8-nodes thermally coupled Eulerian elements, while the tool was considered Lagrangian rigid body.

5.3.1.2 ***Boundary conditions.*** In this study, the three phases of friction stir

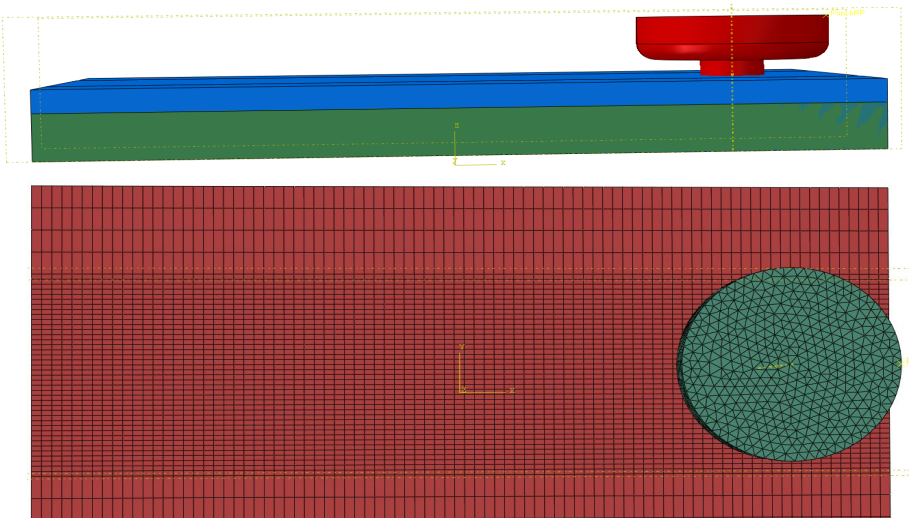

Figure 5.2 Model geometry and mesh

welding were considered in the analysis, which are the plunging phase, dwelling phase, and the welding phase. A reference point was set on the tool at which all the boundary conditions were applied to it. The workpiece was kept fixed during the complete analysis, while the tool was rotating anti-clockwise with a fixed rotational speed throughout the analysis.

In the plunging phase, the tool was set to move in the radial direction through the workpiece until the bottom surface of the shoulder is in contact with the workpiece. The plunging depth was controlled by a constant value equal to the pin length. While in the welding phase, the tool was set to move in the transverse direction with a constant welding speed throughout the step. Two Different rotational speeds were used to study their effect on temperature variation.

5.3.2. Heat generation and heat transfer modelling. As mentioned earlier, during the FSW process, heat is generated by both friction and plastic deformation. In this model, both were considered in the analysis.

The heat of plastic deformation is generated by inelastic work under sticking condition inside the shear layer of the material and can be calculated as in Equation (52).

$$\eta s_{ij} \dot{\varepsilon}_{ij}^{pl} \tag{52}$$

where the percentage of plastic work converting into heat was considered 90%. On the other hand, heat generated by friction was calculated as per Equation (53).

$$q_{surf} = \mu p \dot{\gamma} \tag{53}$$

where μ is the friction coefficient, p the pressure and $\dot{\gamma}$ is the slip rate. In this study, the coefficient of friction was considered a constant value of 0.58 similar to previous works [53, 84]. A modified Coulomb friction law was employed in the model with a shear limit of 167MPa.

In this model, heat transfer is modeled by introducing a type of interaction in Abaqus Explicit called Surface Film Condition. In surface film condition interaction, a film coefficient and a sink temperature are defined. The sink temperature was considered as 25 C for both water and air. The film coefficient acts as a heat transfer coefficient and the values in the model are tabulated in Table 5.1.

Table 5.1 Film Coefficients for FSW and SFSW (W/m.K)

	Workpiece	Tool	Backing Plate
Air	30	30	30
Water	300	300	300

5.3.3. Constitutive model. The material constitutive law that is considered in this model is the Johnson-Cook model (refer to section 3.1.1). Johnson-Cook plasticity model constants used are shown in Table **5.2**.

Table 5.2 Johnson-Cook model constants for Al-5083-O [85]

A (MPa)	B (MPa)	C	n	M	T_{ref} (K)	T_{melt} (K)
170	425	0.0335	0.42	1.225	297	913

5.3.4. Material properties. Thermal properties and Elasticity of AA 5083 are considered as temperature dependent, and inelastic coefficient of 0.9 is considered to convert plastic work into heat. All material properties of AA 5083 used in this model are tabulated in Table **5.3**.

Table 5.3 Thermal and mechanical properties of AA 5083

T (◦C)	ρ (kg m−3)	E (GPa)	ν	Ƙ (W/m.K)	Cp (J kg−1◦C−1)	α(µm m−1◦C−1)
25	2650	72	0.33	121	900	25
100	2650	68.5	0.334	131	933	26.1
149	2630	66.6	0.335	138	955	27.2
204	2620	62.4	0.336	146	985	28.3
260	2620	58.2	0.338	155	1012	29.4
316	2600	54	0.36	161	1040	30.5
371	2600	49.8	0.4	171	1068	31.6
427	2570	34.4	0.41	178	1100	32.7
482		25.9	0.42		1123	

5.4. Results and Discussion

5.4.1. Temperature. Friction Stir Welding (FSW) was compared to Submerged Friction Stir Welding (SFSW) in terms of temperature variation in time.

In order to study the effect of the coolant on temperature variation, two simulations were conducted. In both simulations, the tool rotational speed was fixed to 1700 rpm, and the welding speed was fixed to 75 mm/min. The results show a higher cooling rate in the case of SFSW when compared to In-air FSW as shown in Figure 5.3, and that is due to the fact that, the high heat capacity of water allows to transfer the heat from the TMAZ and HAZ regions, and consequently reduces peak temperatures. It can be seen that, the simulated results are very close to the obtained experimental ones, with lower temperature values in the case of SFSW. This is due to the method of modelling heat transfer, as a sink of constant temperature was considered, while in reality the temperature of water increases due to the heat from the welding process.

In **Figure 5.3**, in both FSW & SFSW, slightly higher temperature rates were captured in the advancing side than in the retreating side of the weld zone, due to the fact that, the relative movement of material flow to the tool rotations leads to a higher plastic strain and thus higher heat dissipation in the AS than in the RS.

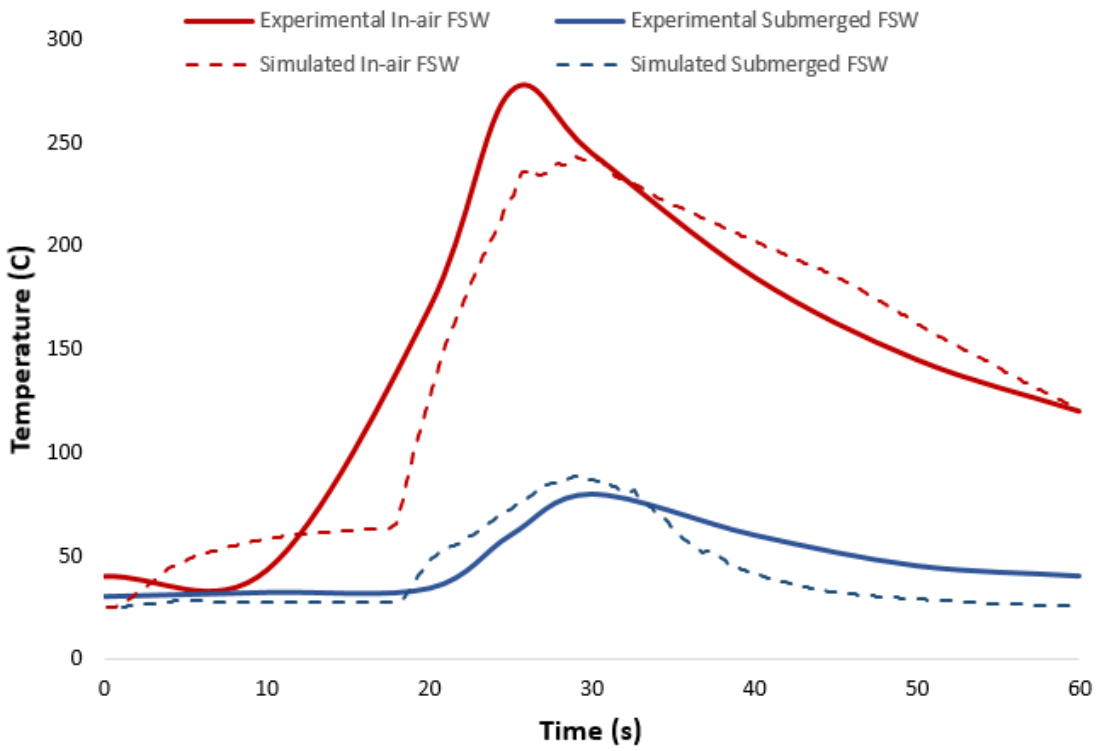

Figure 5.3 Comparison of temperature variation in FSW & SFSW between simulated and experimental results

In addition, in the AS, the material has higher velocity and higher shearing rate than in the RS, which results in higher temperatures in the AS than in the RS, which is in line with the literature [25, 33]. Furthermore, as shown in **Figure 5.4** a and b, as the tool moves in the transverse direction, it faces low-temperature material and disposes it at the RS, which results in lowering the temperature in the RS and raising the temperature in the AS. For the SFSW Process (see **Figure 5.4**a), the temperature decreases rapidly in the transverse direction away from the tool, if compared to FSW (see **Figure 5.4**b). That is due to the fact that, the heat is generated mainly at the contact area between the shoulder and the workpiece, and then transferred to other regions, decreasing gradually as we move away from the shoulder. It can be seen that the temperature gradient in SFSW (see **Figure 5.5**a) is higher than in FSW (see **Figure 5.5**b), due to the high convection coefficient between the workpiece and the water, when compared to the convection coefficient between the workpiece and air. Also, the model predicted very well the flash formation in the SFSW process, which is similar to the one obtained by Kishta and Darras.

In order to observe the temperature history during the FSW and SFSW processes, temperature variation with respect to time has been recorded in four different nodal points in the workpiece. Two points were considered in the advancing side, and two in the retreating side as shown in Figure 5.6. These nodal points are considered on a cross-sectional area 28 mm away from the initial plunging position, and at the surface of the workpiece.

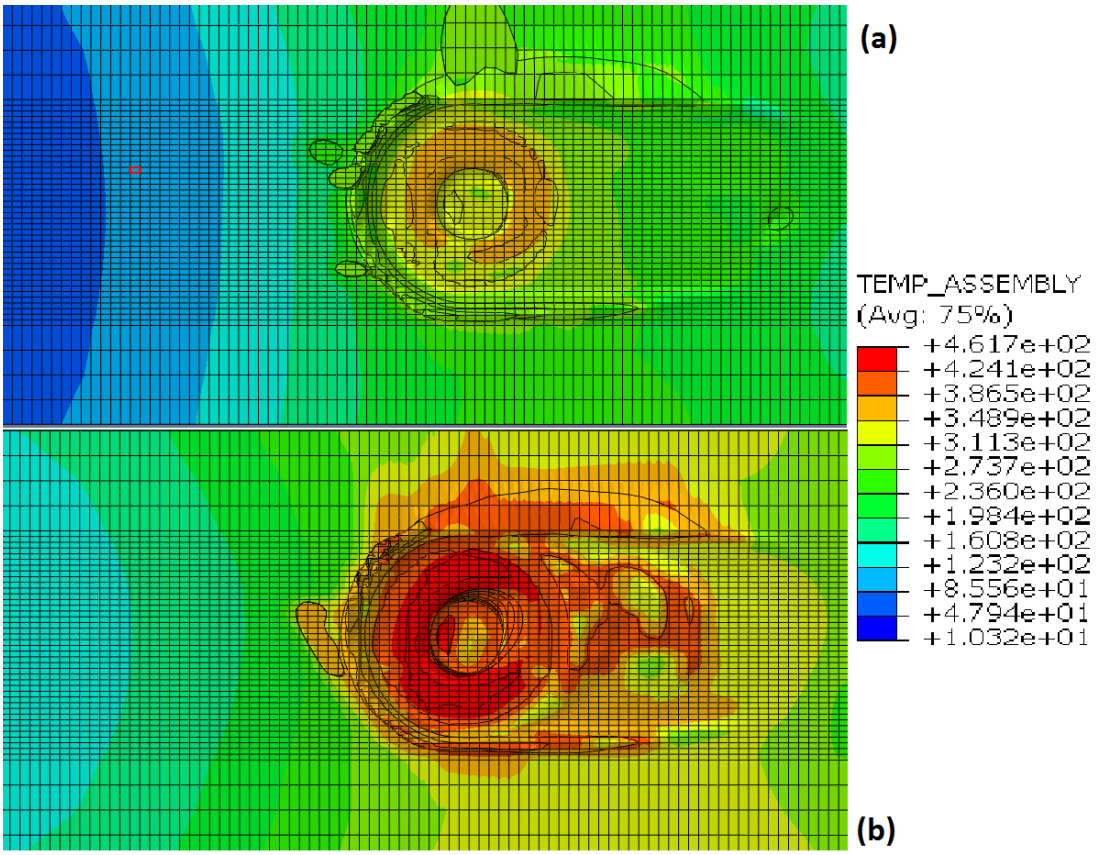

Figure 5.4 Comparison of temperature profile between FSW & SFSW: (a) Top view of SFSW, (b) Top view of FSW

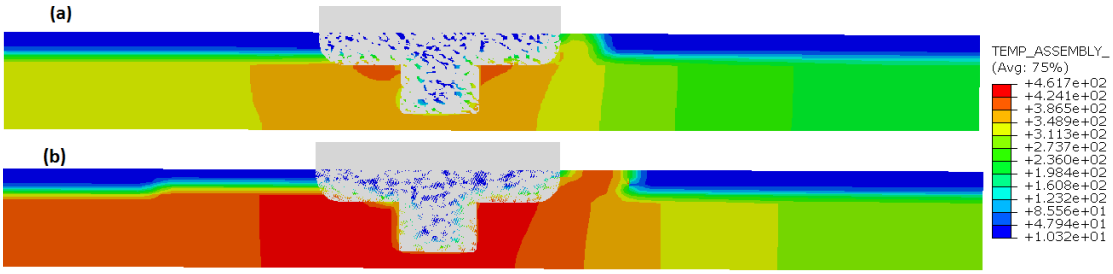

Figure 5.5 Comparison of temperature profile between FSW & SFSW: (a) Side view of SFSW, (b) Side view of FSW

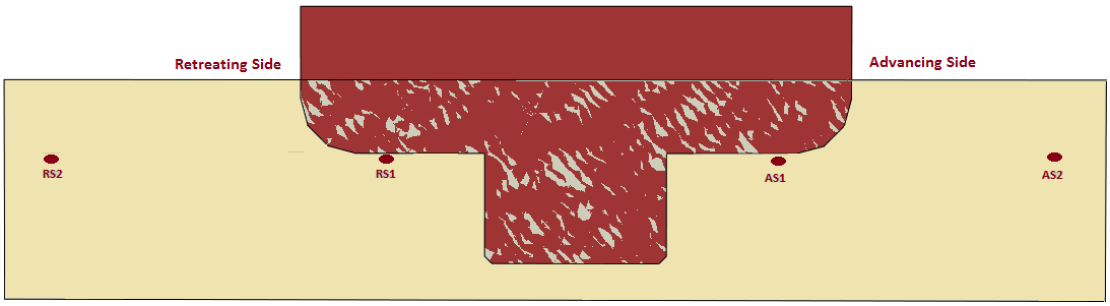

Figure 5.6 Location of Nodal points for Temperature monitoring

The thermal histories for the FSW and SFSW processes at the specified nodal points are shown in Figure 5.7 and Figure 5.8 respectively.

The nodal points AS-1 and RS-1 are in the TMAZ zone, whereas AS-2 and RS-2 are in the HAZ zone. It can be seen that the thermal cycles of the nodes in the advancing side are slightly higher than the corresponding nodes in the retreating side for both FSW and SFSW. Furthermore, the heating and cooling rates are higher for the nodes near to the tool and decrease gradually when considering the nodes away from the tool, which is in line with the literature [86, 87]. Also, it was observed from the model results that 20%-30% reduction in peak temperatures was recorded when using SFSW instead of FSW at this process parameters. Moreover, the peak temperature in the RS is approximately 7% less than the AS for FSW, while for SFSW it is around 14% less.

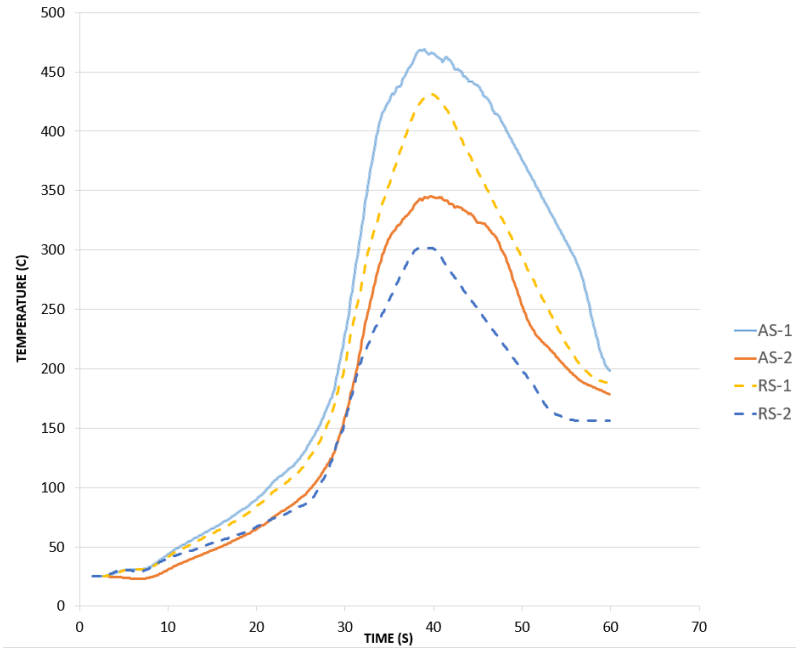

Figure 5.7 Thermal histories for the nodal points shown in Figure 5.6 for FSW

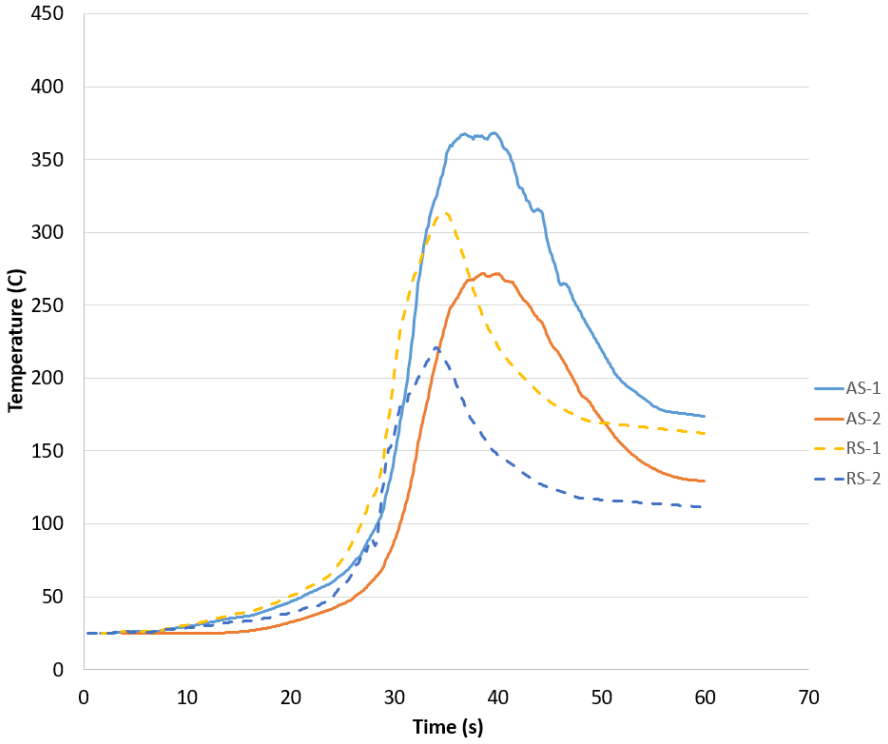

Figure 5.8 Thermal histories for the nodal points shown in Figure 5.6 for SFSW

5.4.2. Effect of tool rotational speed on SFSW. To observe the effect of the tool rotational speed on temperature variation during the SFSW process, two values were considered in the study. Figure **5.9** presents the effect of the tool speed in temperature variation during SFSW process. It is clear that the tool rotational speed directly affects the heat input, as higher speeds lead to higher friction and higher plastic deformation, and thus higher temperatures. As a result, the tool rotational speed plays a major role in material flow and the stirring process, as low rotational speed may result in insufficient material softening, and thus incomplete stirring process. In contrary, high tool rotational speed may lead to good material flow and weld quality, but compromising the mechanical properties of the material due to grain growth that results from high temperatures.

In SFSW, peak temperatures can be reduced due to the high cooling rate of water, and so limiting the grain growth while maintaining high rotational speed, which results in good weld quality and material flow [22].

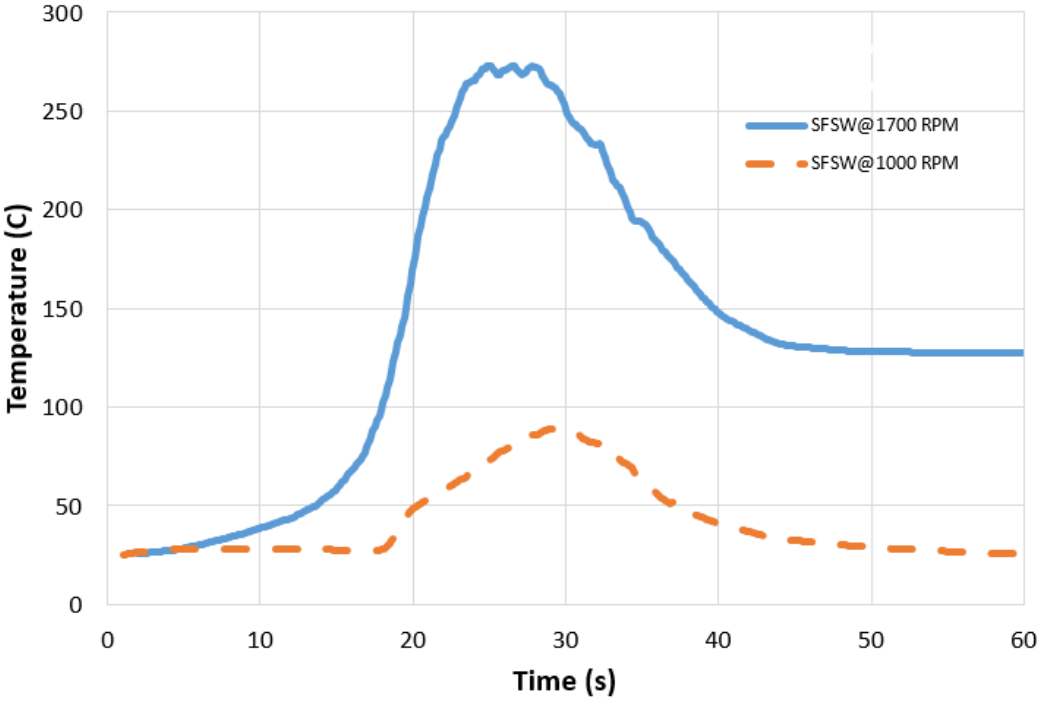

Figure 5.9 Tool rotational speed effect on temperature for SFSW process of AA5083 Aluminum alloy.

Chapter 6. Conclusion and Future Work

In this research, a 3D coupled thermo-mechanical finite element model for AA 5083 was developed in ABAQUS Explicit software, by using CEL technique to model the FSW and SFSW processes. Modified Coulomb friction law was used to define the contact state at the tool-workpiece interface, while Johnson-Cook constitutive law was used to predict material behavior. By using the CEL technique, the tool was modelled as Lagrangian solid body, while the workpiece was modelled as a Eulerian thermally-coupled body. The model well predicted the temperature profile and distribution in both FSW and SFSW processes, being the first model developed to simulate SFSW process. Plus, the model visualized the material flow and flash generation properly. The model was validated against the experimental investigation done by Kishta & Darras, by comparing the temperature variation between FSW and SFSW at 1000 rpm tool rotational speed and 75 mm/min welding speed. Results show that simulated temperature values are close to the ones obtained by the experiment, but lower. That is due to considering constant sink temperature in the model, while actually the cooling fluid temperature increases during the process.

The thermal histories in FSW and SFSW processes were studied considering a tool rotational speed of 1700 rpm, and 75 mm/min welding speed for both processes. It was observed that, 20% -30% reduction in peak temperature values was recorded when using SFSW process. The width of the HAZ region was reduced considerably when using SFSW, due to the high effect of heat transfer at this region, as no plastic deformation exist in it. Also, a slight temperature reduction was recorded in the RS when compared to the AS. This reduction is doubled in the case of SFSW process reaching 14%. The effect of the tool rotational speed on temperature in SFSW process was investigated. It was found that, increasing the tool rotational speed from 1000 rpm to 1700 rpm, resulted in rising the peak temperature by 200%. This temperature rise may have a major impact in improving the weld quality during the process.

Future Work

The proposed future work is to investigate the effect of using SFSW process in grain size and Microhardness. Also, to evaluate the optimum process parameters (welding speed and rotational speed) required to achieve good weld quality and better mechanical properties during SFSW process.

References

[1] R. S. Mishra and Z. Y. Ma, "Friction stir welding and processing," *Materials Science and Engineering R,* vol. 50, no. 1, pp. 1-78, 2005.

[2] K. Masaki, Y. S. Sato, M. Maeda, and H. Kokawa, "Experimental simulation of recrystallized microstructure in friction stir welded Al alloy using a plane-strain compression test," *Scripta Materialia,* vol. 58, pp. 355-360, March 2008.

[3] H. N. B. Schmidt and J. Hattel, "Modelling thermomechanical conditions at the tool/matrix interface in Friction Stir Welding," in *Proc. of 5th International Friction Stir Welding Symposium*, 2004.

[4] B. Darras, M. Khraisheh, F. Abu-Farha, and M. Omar, "Friction stir processing of commercial AZ31 magnesium alloy," *Journal of Materials Processing Technology,* vol. 191, no. 1-3, pp. 77-81, 2007.

[5] B. M. Darras, M. Omar, and M. K. Khraisheh, "Experimental thermal analysis of friction stir processing," in *Materials Science Forum*, vol. 539: Trans Tech Publ, pp. 3801-3806, 2007.

[6] K. V. Jata and S. L. Semiatin, "Continuous dynamic recrystallization during friction stir welding of high strength aluminum alloys," *Scripta Materialia,* vol. 43, no. 8, pp. 743-749, September 2000.

[7] B. M. Darras, "A model to predict the resulting grain size of friction-stir-processed AZ31 magnesium alloy," *Journal of Materials Engineering and Performance,* vol. 21, no. 7, pp. 1243-1248, 2012.

[8] B. Darras and M. Khraisheh, "Analytical modeling of strain rate distribution during friction stir processing," *Journal of Materials Engineering and Performance,* vol. 17, no. 2, pp. 168-177, 2008

[9] P. Ulysse, "Three-dimensional modeling of the friction stir-welding process," *International Journal of Machine Tools and Manufacture,* vol. 42, no. 14, pp. 1549-1557, November 2002.

[10] C. Chen and R. Kovacevic, "Finite element modeling of friction stir welding—thermal and thermomechanical analysis," *International Journal of Machine Tools and Manufacture,* vol. 43, no. 13, pp. 1319-1326, 2003

[11] X. Deng and S. Xu, "Two-Dimensional Finite Element Simulation of Material Flow in the Friction Stir Welding Process," *Journal of Manufacturing Processes,* vol. 6, no. 2, pp. 125-133, 2004.

[12] P. A. Colegrove and H. R. Shercliff, "3-Dimensional CFD modelling of flow round a threaded friction stir welding tool profile," *Journal of Materials Processing Technology,* vol. 169, no. 2, pp. 320-327, 2005.

[13] T. De Vuyst, L. D'Alvise, A. Simar, B. De Meester, and S. Pierret, "Finite element modelling of friction stir welding of aluminium alloy plates-inverse analysis using a genetic algorithm," *International Institute of Welding*, vol. 49, pp. 47-55, 2005.

[14] V. Soundararajan, S. Zekovic, and R. Kovacevic, "Thermo-mechanical model with adaptive boundary conditions for friction stir welding of Al 6061," *International Journal of Machine Tools and Manufacture,* vol. 45, no. 14, pp. 1577-1587, 2005.

[15] H. W. Zhang, Z. Zhang, and J. T. Chen, "The finite element simulation of the friction stir welding process," *Materials Science and Engineering A,* vol. 403, no. 1-2, pp. 340-348, 2005

[16] E. E. Kishta, A. Farid, and B. Darras, "Nonlinear Finite Element Simulation of Friction Stir Processing of Marine Grade 5083 Aluminum Alloy," *Engineering Transactions,* vol. 62, no. 4, pp. 313–328, 2014.

[17] W. Pan, D. Li, A. M. Tartakovsky, S. Ahzi, M. Khraisheh, and M. Khaleel, "A new smoothed particle hydrodynamics non-Newtonian model for friction stir welding: Process modeling and simulation of microstructure evolution in a magnesium alloy," *International Journal of Plasticity,* vol. 48, pp. 189-204, 2013.

[18] A. Timesli, B. Braikat, H. Lahmam, and H. Zahrouni, "A new algorithm based on Moving Least Square method to simulate material mixing in friction stir welding," *Engineering Analysis With Boundary Elements,* vol. 50, pp. 372-380, 2015.

[19] C. T. Wu, W. Hu, H. P. Wang, and H. S. Lu, "A Robust Numerical Procedure for the Thermomechanical Flow Simulation of Friction Stir Welding Process Using an Adaptive Element-Free Galerkin Method," *Mathematical Problems in Engineering,* vol. 2015, pp. 1-16, 2015.

[20] G. Yoshikawa, F. Miyasaka, Y. Hirata, Y. Katayama, and T. Fuse, "Development of numerical simulation model for FSW employing particle method," *Science and Technology of Welding and Joining,* vol. 17, no. 4, pp. 255-263, 2012.

[21] Y. Xiao, H. Zhan, Y. Gu, and Q. Li, "Modeling heat transfer during friction stir welding using a meshless particle method," *International Journal of Heat and Mass Transfer,* vol. 104, pp. 288-300, January 2017.

[22] E. E. Kishta and B. Darras, "Experimental investigation of underwater friction-stir welding of 5083 marine-grade aluminum alloy," *Proceedings of the Institution of Mechanical Engineers, Part B: Journal of Engineering Manufacture,* vol. 230, no. 3, pp. 458-465, 2016.

[23] A. H. J. Donea, J.-Ph. Ponthot and A. Rodrıguez-Ferran, "Arbitrary Lagrangian–Eulerian Methods," in *Encyclopedia of Computational Mechanics* vol. 1, 2004.

[24] M. Chiumenti, M. Cervera, C. Agelet de Saracibar, and N. Dialami, "Numerical modeling of friction stir welding processes," *Computer Methods in Applied Mechanics and Engineering,* vol. 254, pp. 353-369, February 2013.

[25] H.-H. Cho *et al.*, "Three-dimensional numerical and experimental investigation on friction stir welding processes of ferritic stainless steel," *Acta Materialia,* vol. 61, no. 7, pp. 2649-2661, 2013

[26] A. Hasan, C. Bennett, and P. Shipway, "A numerical comparison of the flow behaviour in Friction Stir Welding (FSW) using unworn and worn tool geometries," *Materials and Design,* vol. 87, pp. 1037-1046, 2015

[27] D. Kim *et al.*, "Numerical simulation of friction stir butt welding process for AA5083-H18 sheets," *European Journal of Mechanics / A Solids,* vol. 29, no. 2, pp. 204-215, 2010

[28] R. Nandan, G. G. Roy, T. J. Lienert, and T. Debroy, "Three-dimensional heat and material flow during friction stir welding of mild steel," *Acta Materialia,* vol. 55, no. 3, pp. 883-895, 2007.

[29] H. W. Nassar and M. K. Khraisheh, "Simulation of Material Flow and Heat Evolution in Friction Stir Processing Incorporating Melting," *Journal of Engineering Materials and Technology-Transactions of the ASME,* vol. 134, no. 4, 2012.

[30] S. Pal and M. Phaniraj, "Determination of heat partition between tool and workpiece during FSW of SS304 using 3D CFD modeling," *Journal of Materials Processing Technology,* vol. 222, pp. 280-286, 2015.

[31] H. Su, C. S. Wu, M. Bachmann, and M. Rethmeier, "Numerical modeling for the effect of pin profiles on thermal and material flow characteristics in friction stir welding," *Materials and Design,* vol. 77, pp. 114-125, 2015

[32] C.WU, W. Zhang, S. Lei, and M. CHEN, "Visualization and simulation of plastic material flow in friction stir welding of 2024 aluminium alloy plates," *Transactions of Nonferrous Metals Society of China,* vol. 22, no. 6, pp. 1445-1451, 2012

[33] J. Zhang *et al.*, "Numerical simulation and experimental investigation on friction stir welding of 6061-T6 aluminum alloy," *Materials and Design,* vol. 60, pp. 94-101, August 2014.

[34] S. Aljoaba, O. Dillon, M. Khraisheh, and I. Jawahir, "Modeling the effects of coolant application in friction stir processing on material microstructure using 3D CFD analysis," *Journal of Materials Engineering and Performance,* vol. 21, no. 7, pp. 1141-1150, 2012.

[35] C. M. S. W. J. M. Tegart, "Hot Workability," *International Metallurgical Reviews,* vol. 17, no. 1, pp. 1-24, 1972.

[36] A. H. Ammouri and R. F. Hamade, "On the selection of constitutive equation for modeling the friction stir processes of twin roll cast wrought AZ31B," *Materials and Design,* vol. 57, pp. 673-688, 2014

[37] C. I. Chang, C. J. Lee, and J. C. Huang, "Relationship between grain size and Zener–Holloman parameter during friction stir processing in AZ31 Mg alloys," *Scripta Materialia,* vol. 51, no. 6, pp. 509-514, 2004.

[38] A. Gerlich, M. Yamamoto, and T. North, "Strain rates and grain growth in Al 5754 and Al 6061 friction stir spot welds," *Metallurgical and Materials Transactions A,* vol. 38, no. 6, pp. 1291-1302, 2007.

[39] M. Guerra, C. Schmidt, J. McClure, L. Murr, and A. Nunes, "Flow patterns during friction stir welding," *Materials Characterization,* vol. 49, no. 2, pp. 95-101, 2002.

[40] Y. Zhu, G. Chen, Q. Chen, G. Zhang, and Q. Shi, "Simulation of material plastic flow driven by non-uniform friction force during friction stir welding and related defect prediction," *Materials and Design,* vol. 108, pp. 400-410, October 2016.

[41] Y. Dong, K. A. Tagavi, M. R. Lovell, and Z. Deng, "Analysis of stress in cross wedge rolling with application to failure," *International Journal of Mechanical Sciences,* vol. 42, no. 7, pp. 1233-1253, January 2000.

[42] A. Hasan, C. Bennett, P. Shipway, S. Cater, and J. Martin, "A numerical methodology for predicting tool wear in Friction Stir Welding," *Journal of Materials Processing Technology,* vol. 241, pp. 129-140, 2017.

[43] G. R. Liu and M. B. Liu, *Smoothed Particle Hydrodynamics: A Meshfree Particle Method*. World Scientific, 2003.

[44] M. Z. H. Khandkar, J. A. Khan, A. P. Reynolds, and M. A. Sutton, "Predicting residual thermal stresses in friction stir welded metals," *Journal of Materials Processing Technology,* vol. 174, no. 1, pp. 195-203, May 2006.

[45] L. Fratini, G. Buffa, and R. Shivpuri, "Improving friction stir welding of blanks of different thicknesses," *Materials Science and Engineering: A,* vol. 459, no. 1, pp. 209-215, 2007.

[46] M. Khandkar, J. A. Khan, and A. P. Reynolds, "Prediction of temperature distribution and thermal history during friction stir welding: input torque based model," *Science and Technology of Welding and Joining,* vol. 8, no. 3, pp. 165-174, 2003

[47] G. Buffa, L. Fratini, and M. Piacentini, "On the influence of tool path in friction stir spot welding of aluminum alloys," *Journal of Materials Processing Technology,* vol. 208, no. 1, pp. 309-317, November 2008.

[48] G. Buffa, J. Hua, R. Shivpuri, and L. Fratini, "A continuum based fem model for friction stir welding—model development," *Materials Science and Engineering,* vol. A 419, 2006.

[49] L. Fratini, G. Buffa, D. Palmeri, J. Hua, and R. Shivpuri, "Material flow in FSW of AA7075-T6 butt joints: continuous dynamic recrystallization phenomena," *Journal of Engineering Materials and Technology,* vol. 128, no. 3, pp. 428-435, 2006.

[50] W. F. Noh, "CEL: A time-dependent, two-space-dimensional, coupled Eulerian-Lagrange code," Lawrence Radiation Lab., Univ. of California, Livermore, 1963.

[51] Xiamen, "Engineering Management and Industrial Engineering," in *International Conference on Engineering Management and Industrial Engineering (EMIE 2014)*, China, 2014.

[52] D. J. Benson, "Computational Methods in Lagrangian and Eulerian Hydrocodes," *Computer Methods in Applied Mechanics and Engineering,* vol. 99, no. 2-3, pp. 235-394, 1992.

[53] F. Al-Badour, N. Merah, A. Shuaib, and A. Bazoune, "Coupled Eulerian Lagrangian finite element modeling of friction stir welding processes," *Journal of Materials Processing Technology,* vol. 213, no. 8, pp. 1433-1439, 2013.

[54] V. Malik, N. K. Sanjeev, H. S. Hebbar, and S. V. Kailas, "Time Efficient Simulations of Plunge and Dwell Phase of FSW and its Significance in FSSW," *Procedia Materials Science,* vol. 5, pp. 630-639, 2014.

[55] M. Grujicic, R. Yavari, S. Ramaswami, J. Snipes, and R. Galgalikar, "Computational analysis of inter-material mixing and weld-flaw formation during dissimilar-filler-metal friction stir welding (FSW) null," *Multidiscipline Modeling in Materials and Structures,* vol. 11, no. 3, pp. 322-349, October 2015.

[56] M. Grujicic, T. He, G. Arakere, H. V. Yalavarthy, C. F. Yen, and B. A. Cheeseman, "Fully coupled thermomechanical finite element analysis of material evolution during friction-stir welding of AA5083," *Proceedings Of The Institution of Mechanical Engineers Part B-Journal of Engineering Manufacture,* vol. 224, pp. 609-625, 2010.

[57] M. Grujicic, B. Pandurangan, C. f. Yen, and B. A. Cheeseman, "Modifications in the AA5083 Johnson-Cook Material Model for Use in Friction Stir Welding Computational Analyses," *Journal of Materials Engineering and Performance,* vol. 21, no. 11, pp. 2207-2217, 2012.

[58] F. J. Zerilli and R. W. Armstrong, "Dislocation-mechanics-based constitutive relations for material dynamics calculations," *Journal of Applied Physics,* vol. 61, no. 5, pp. 1816, 1987.

[59] F. J. Zerilli, "Dislocation mechanics-based constitutive equations," *Metallurgical and Materials Transactions A,* vol. 35, no. 9, pp. 2547-2555, 2004.

[60] T. Mirzaie, H. Mirzadeh, and J. M. Cabrera, "A simple Zerilli-Armstrong constitutive equation for modeling and prediction of hot deformation flow stress of steels," *Mechanics of Materials,* vol. 94, pp. 38-45, 2016.

[61] H. Y. Zhan, G. Wang, D. Kent, and M. Dargusch, "Constitutive modelling of the flow behaviour of a beta titanium alloy at high strain rates and elevated temperatures using the Johnson-Cook and modified Zerilli-Armstrong models," *Materials Science and Engineering A-Structural Materials Properties Microstructure and Processing,* vol. 612, pp. 71-79, 2014.

[62] H. Zhang, W. Wen, H. Cui, and Y. Xu, "A modified Zerilli–Armstrong model for alloy IC10 over a wide range of temperatures and strain rates," *Materials Science and Engineering A,* vol. 527, no. 1, pp. 328-333, 2009.

[63] Z. Zhang, "Comparison of two contact models in the simulation of friction stir welding process," *Journal of Materials Science,* vol. 43, no. 17, pp. 5867-5877, 2008.

[64] M. Assidi, L. Fourment, S. Guerdoux, and T. Nelson, "Friction model for friction stir welding process simulation: Calibrations from welding experiments," *International Journal of Machine Tools and Manufacture,* vol. 50, no. 2, pp. 143-155, 2010.

[65] M. Grujicic, S. Ramaswami, J. S. Snipes, V. Avuthu, R. Galgalikar, and Z. Zhang, "Prediction of the Grain-Microstructure Evolution Within a Friction Stir Welding (FSW) Joint via the Use of the Monte Carlo Simulation Method," *Journal of Materials Engineering and Performance,* vol. 24, no. 9, pp. 3471-3486, 2015.

[66] H. Schmidt and J. Hattel, "Modelling heat flow around tool probe in friction stir welding," *Science & Technology of Welding and Joining,* vol. 10, no. 2, 2005.

[67] C. Hamilton, S. Dymek, and M. Blicharski, "A model of material flow during friction stir welding," *Materials Characterization,* vol. 59, no. 9, pp. 1206-1214, September 2008.

[68] M. Song, R. Kovacevic, J. Ouyang, and M. Valant, "A Detailed Three-Dimensional Transient Heat Transfer Model for Friction Stir Welding," in *6th International Trends in Welding Research Conference, pp.212-217, April 2002*.

[69] S. Guerdoux and L. Fourment, "A 3D numerical simulation of different phases of friction stir welding," *Modelling and Simulation In Materials Science And Engineering,* vol. 17, no. 7, July 2009.

[70] H. Schmidt and J. Hattel, "A local model for the thermomechanical conditions in friction stir welding," *Modelling and Simulation in Materials Science and Engineering,* vol. 13, no. 1, pp. 77-93, 2005.

[71] G.-R. Liu, *Mesh Free Methods: Moving Beyond The Finite Element Method*. CRC press, 2002.

[72] L. B. Lucy, "A numerical approach to the testing of the fission hypothesis," *The Astronomical Journal,* vol. 82, pp. 1013-1024, 1977.

[73] P. W. Randles and L. D. Libersky, "Smoothed Particle Hydrodynamics: Some recent improvements and applications," *Computer Methods in Applied Mechanics and Engineering,* vol. 139, no. 1–4, pp. 375-408, 1996.

[74] T. Belytschko, Y. Y. Lu, and L. Gu, "Element-Free Galerkin Methods," *International Journal For Numerical Methods In Engineering,* vol. 37, no. 2, pp. 229-256, 1994.

[75] B. Nayroles, G. Touzot, and P. Villon, "Generalizing the finite element method: Diffuse approximation and diffuse elements," *Computational Mechanics,* vol. 10, no. 5, pp. 307-318, 1992.

[76] D. C. Simkins and S. Li, "Meshfree simulations of thermo-mechanical ductile fracture," *Computational Mechanics,* vol. 38, no. 3, pp. 235-249, 2006.

[77] H. Liu, H. Fujii, M. Maeda, and K. Nogi, "Tensile properties and fracture locations of friction-stir-welded joints of 2017-T351 aluminum alloy," *Journal of Materials Processing Technology*, vol. 142, no. 3, pp. 692-696, 2003.

[78] W. Baeslack, K. Jata, and T. J. Lienert, "Structure, properties and fracture of friction stir welds in a high-temperature Al-8.5 Fe-1.3 V–1.7 Si alloy (AA-8009)," *Journal of Materials Science,* vol. 41, no. 10, pp. 2939-2951, 2006.

[79] M. Cabibbo, H. McQueen, E. Evangelista, S. Spigarelli, M. Di Paola, and A. Falchero, "Microstructure and mechanical property studies of AA6056 friction stir welded plate," *Materials Science and Engineering: A,* vol. 460, pp. 86-94, 2007.

[80] H. Zhang, H. Liu, and L. Yu, "Microstructure and mechanical properties as a function of rotation speed in underwater friction stir welded aluminum alloy joints," *Materials and Design*, vol. 32, no. 8-9, pp. 4402-4407, 2011.

[81] T. Nelson, R. Steel, and W. J. Arbegast, "In situ thermal studies and post-weld mechanical properties of friction stir welds in age hardenable aluminium alloys," *Science and Technology of Welding And Joining*, vol. 8, no. 4, pp. 283-288, August 2003.

[82] W. F. Xu, J. H. Liu, D. L. Chen, G. H. Luan, and J. S. Yao, "Improvements of strength and ductility in aluminum alloy joints via rapid cooling during friction stir welding," *Materials Science and Engineering: A,* vol. 548, pp. 89-98, June 2012.

[83] M. A. Wahid, Z. A. Khan, and A. N. Siddiquee, "Review on underwater friction stir welding: A variant of friction stir welding with great potential of improving joint properties," *Transactions of Nonferrous Metals Society of China,* vol. 28, no. 2, pp. 193-219, 2018.

[84] Z. Zhu, M. Wang, H. Zhang, X. Zhang, T. Yu, and Z. Wu, "A finite element model to simulate defect formation during friction stir welding," *Metals,* vol. 7, no. 7, p. 256, 2017.

[85] F. Al-Badour, N. Merah, A. Shuaib, and A. Bazoune, "Thermo-mechanical finite element model of friction stir welding of dissimilar alloys," *The International Journal of Advanced Manufacturing Technology,* vol. 72, no. 5-8, pp. 607-617, 2014.

[86] B. Ahmad, A. Galloway, and A. Toumpis, "Advanced numerical modelling of friction stir welded low alloy steel," *Journal of Manufacturing Processes,* vol. 34, pp. 625-636, 2018.

[87] R. Nandan, G. Roy, T. Lienert, and T. DebRoy, "Numerical modelling of 3D plastic flow and heat transfer during friction stir welding of stainless steel," *Science and Technology of Welding and Joining,* vol. 11, no. 5, pp. 526-537, 2006.

Vita

Mohamed Anass was born in 1992, in Sudan. He received his primary and secondary education in Wad Medani, Sudan. He received his B.Sc. degree in Mechanical Engineering from the University of Khartoum in 2013. From 2013 to 2014, he worked as a Teaching Assistant at the University of Khartoum. Then, from 2014 to 2015, he worked as a Mechanical Design Engineer in KETS.

In September 2015, he joined the Mechanical Engineering master's program in the American University of Sharjah as a graduate teaching assistant. During his master's study, he co-authored one paper which is presented at an international conference. His research interests are in Friction Stir Welding and Finite Element Analysis.